Journal of Materials Chemistry C

ROYAL SOCIETY OF CHEMISTRY

REVIEW

View Article Online
View Journal | View Issue

Cite this: J. Mater. Chem. C, 2024, 12, 15359

Liquid crystal elastomers in soft micro electromechanical systems: a review of recent developments

Elaheh Asgari, *[a] Alexandre Robichaud,[b] Paul-Vahé Cicek[c] and Andy Shih[a]

Liquid crystal elastomers (LCEs) are a class of electroactive polymers (EAPs) that have attracted significant attention in the microelectromechanical system (MEMS) community due to their unique combination of properties, including different actuation mechanisms, high generated strain (up to 400%), preprogrammed deformation, and biocompatibility. LCEs have the potential to revolutionize MEMS devices by enabling the development of miniaturized actuators, sensors, and other functional components with enhanced performance. This review provides a comprehensive overview of LCE-based devices for MEMS applications. It begins by exploring the fundamentals of LCEs, delving into their core component, liquid crystals (LCs). Subsequently, it examines the LCE preparation process, encompassing synthesis techniques, and alignment mechanisms. The review then delves into the state-of-the-art LCE-based devices used in MEMS, discussing their functionalities, characterization, and fabrication methods. A particular focus is placed on cutting-edge methods for integrating LCEs with MEMS using compatible fabrication techniques. Looking towards the future, the review introduces ionic liquid crystal elastomers (iLCEs) as a promising novel class of LCE-based materials with the potential to address limitations and enhance the performance of conventional LCEs in MEMS. Finally, a conclusion lays out future research orientations in iLCE-based MEMS technologies and the challenges that remain to be addressed in order to further expand their applications.

Received 31st July 2024,
Accepted 16th September 2024

DOI: 10.1039/d4tc03282a

rsc.li/materials-c

[a] Department of Electrical Engineering, École de Technologie Supérieure (ETS), Montreal, QC H3C 1K3, Canada. E-mail: Elaheh.asgari.1@ens.etsmtl.ca
[b] Department of Applied Sciences, Université du Québec à Chicoutimi (UQAC), Chicoutimi, QC G7H 2B1, Canada
[c] Microtechnologies Integration & Convergence Research Group, Université du Québec à Montréal (UQAM), Montreal, QC H2X 3Y7, Canada

1. Introduction

Soft micro-electromechanical systems (soft MEMS) are emerging as a transformative field, challenging the conventional paradigms of traditional MEMS devices. While MEMS have always been synonymous with precision engineering and

Elaheh Asgari

Elaheh Asgari is a PhD candidate at École de Technologie Supérieure (ETS) in Montreal, Canada. She received her BEng degree from the University of Tabriz, Iran, in 2019, and continued her studies at Sahand University of Technology, where she obtained her MEng degree in Electrical Engineering-Nano and Microelectronic Devices in 2021. Her current research focuses on the development of novel soft MEMS using LCE-based materials for biomedical applications.

Alexandre Robichaud

Alexandre Robichaud received a PhD degree in electrical engineering from the École de technologie supérieure, Montreal, QC, Canada, in 2020. He has held scholarships from the Natural Sciences and Engineering Research Council of Canada (NSERC) and the Quebec Fund for Research in Nature and Technology (FRQNT). In 2019, he joined the Université du Québec à Chicoutimi (UQAC), Chicoutimi, QC, Canada, where he is a Professor in Electrical and Computer Engineering. His research interests include MEMS and analog microelectronics.

miniaturization, their reliance on inherently rigid ceramics and inorganic semiconductors – such as silicon, gallium arsenide, and gallium nitride[1] – has hindered the development of devices that can operate on flexible substrates. Addressing such limitations by means of soft MEMS can enable conformability to irregular shapes, adaptability to dynamic environments, and new complex motion patterns.

Since 2007, many materials have surfaced as candidates for soft MEMS including composite elastomer conductors, flexible nanomaterials, and organic materials.[2–9] In particular, electroactive polymers (EAPs) are able to conform to irregular shapes, seamlessly adapt to dynamic environments, and sustain a wide range of intricate movements.[10] The appeal of EAPs lies in their remarkable combination of properties: substantial deformation upon electrical stimulation, simple fabrication processes, and inherent flexibility.[10–12] This unique synergy paves the way for a broad spectrum of innovative applications in soft MEMS.[10] Through the use of various EAPs, a wide range of soft MEMS applications have been demonstrated, including self-regulating iris,[13] tunable iris-like apertures,[14] micro-grippers,[15] peristaltic micropumps,[16] microvalves,[17] micro-pillars,[18] and tunable optical lenses.[19] Dong *et al.* (2006) exploited the tunable actuation properties of EAP to create a microfluidic liquid lens with tunable focal length (from $-\infty$ to $+\infty$ divergence and convergence), as shown in Fig. 1(i).[19] Their design utilizes a stimuli-responsive EAP, hydrogel, that dynamically modifies the pinned water-oil interface contact angle (θ), thereby controlling the shape of the liquid meniscus. Notably, they employed two types of hydrogels by photopatterning – one responsive to temperature and another to pH variations. Leveraging the advantageous volume change capabilities of EAPs, Eom *et al.* (2017) presented a novel peristaltic micropump powered by serially arranged diaphragm-type dielectric elastomer (DE) actuators.[16] These DE actuators change in volume upon actuation, propelling fluid within a microchannel. The design leverages polydimethylsiloxane (PDMS) as the DE material and utilizes a multi-step photolithography process for integration. Notably, a 55 μm out-of-plane displacement with 2.5 kV applied voltage is achieved. Fig. 1(ii) depicts the micropump schematic and working principle, a single fabricated DE actuator, and the actuator diagram. With their biomimetic potential, EAPs have become valuable tools in soft robotics. Carrico *et al.* (2017) made a breakthrough in soft robotics with a biomimetic 3D-printed ionic polymer–metal composite (IPMC) robot.[20] As shown in Fig. 1(iii), mimicking caterpillar movement, it uses Nafion to print modular, functional body sections. These sections are then activated and plated, becoming smart electroactive components. The key to operation lies in manipulating hydrated IPMC sections with voltage, enabling gripping and body expansion/contraction. This allows the robot to move forward and backward like a caterpillar. Beyond the impressive prototype, the novel 3D-printing process and design methods offer valuable insights for future soft robots.

MEMS integration and device performance necessitate an efficient control interface for microfluidic applications. Haefner *et al.* (2018) presented a novel approach for microfluidic valve control utilizing light-responsive hydrogels.[17] These hydrogels exhibit optothermal actuation, where light exposure triggers conversion to thermal energy. Fabrication begins with defining the desired hydrogel height using spacers sandwiched between two glass slides. A photomask then defines the hydrogel pattern through light-induced polymerization, resulting in an array of hydrogel dots. Following development to remove unpolymerized material, the patterned hydrogel layer is bonded to a glass substrate. Subsequently, a microfluidic chip, previously fabricated *via* soft lithography, is plasma-treated and bonded to this layer, creating a microfluidic device with integrated, light-activated valves. The actuation principle leverages the thermal response of the hydrogels. Illuminating the valves with projector light induces localized heating, leading to hydrogel shrinkage and consequent valve opening.

Paul-Vahé Cicek

Paul-Vahé Cicek received his BEng degree in electrical engineering (minor in arts) and PhD degree in electrical engineering from McGill University, Montreal, QC, Canada, in 2006 and 2016 respectively. In 2014, he joined the Université du Québec à Montréal (UQAM), where he is currently an Associate Professor in microsystems engineering, and directs the Microtechnologies Integration and Convergence Research Group. His research interests include novelty MEMS technologies and devices, digital, analog and mixed electronic circuits, monolithic integration of MEMS and VLSI electronics, advanced packaging and encapsulation, and integrated microfluidics for lab-on-a-chip systems.

Andy Shih

Andy Shih received his BEng and MEng in electrical engineering from McGill University, Canada, in 2011 and 2013, and his PhD in electrical engineering and computer science from MIT (Landsman Fellow) in 2018. He is an Assistant Professor in the Department of Electrical Engineering at ÉTS, Montreal, and a member of IEEE, ReSMiQ, and LaCIME. His research focuses on organic-based electronic devices, including organic electrochemical transistors, neuromorphic circuits, soft MEMS, and printed antenna sensors for wound monitoring, along with generative models for synthetic sensor data.

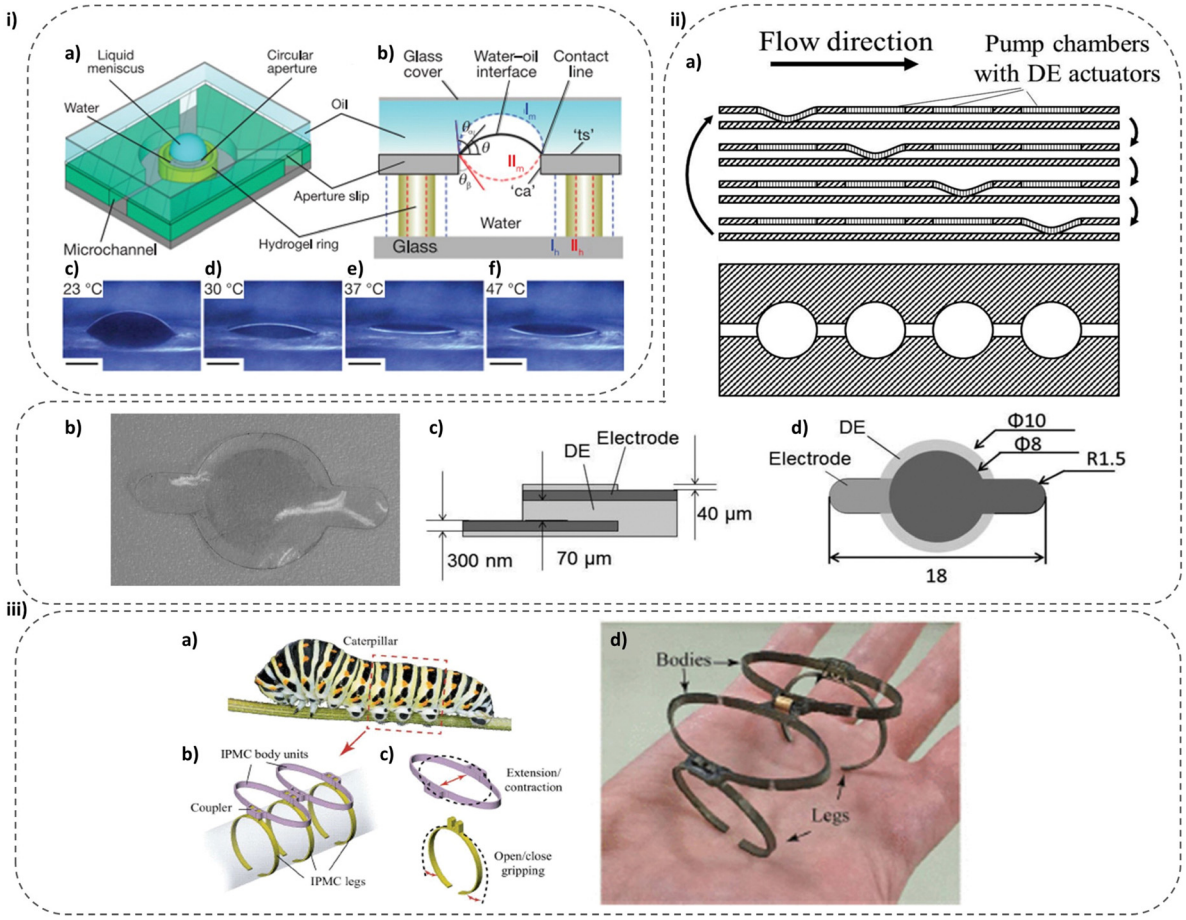

Fig. 1 EAP-based MEMS-based devices: (i) smart micro lens using hydrogel: (a) schematic of the water–oil interface with microfluidic channels. (b) The variable-focus mechanism employs a hydrophilic base ("ca") and a hydrophobic top ("t_s") to stabilize the oil–water interface (θ). The shape of this interface is controlled by the contraction and expansion of a hydrogel, which adjusts the focal length. Blue dashed lines: expanded hydrogel state ("I_h") and corresponding divergent micro lens ("I_m") ($\theta = \theta_\alpha$). Red dashed lines: contracted hydrogel state ("II_h") and associated convergent micro lens ("II_m") ($\theta = -(90 - \theta_\beta)$). (c)–(f) Temperature dependence of the liquid micro lens shape (scale bars: 1.0 mm). (ii) Peristaltic DE micropump: (a) micropump design schematics illustrating the peristaltic micropump's cross-section, working principle, and top view for comprehensive visualization. (b) Fabricated single DE actuator. (c) and (d) Single-layer DE actuator design. (iii) 3D-printed soft crawling IPMC robot: (a) schematic illustration of the biomimetic design principle inspired by a caterpillar's locomotion. (b) Key units of the robot, categorized as body (extensor) and leg (gripper) units, for functional analysis. (c) Modular design of bodies and legs allows for scalable robot construction, facilitating customization for specific applications. (d) High-resolution view of the assembled robot, showcasing the integration of fabricated legs and body parts. (i) Reprinted (adapted) with permission from ref. 19. Copyright 2006 Nature Publishing Group. (ii) Reprinted with permission from ref. 16. Copyright 2017 SPIE, (iii) Reprinted with permission from ref. 20. Copyright 2017, IEEE.

Conversely, turning off the light source allows the hydrogels to swell and close the valves. Fig. 2(i) illustrates the schematic fabrication process for the microfluidic chip and the light-to-heat actuation mechanism, where strategically designed, dot-shaped features facilitate localized hydrogel response upon light exposure.

EAPs offer exciting possibilities for next-generation actuators, as evidenced by Terasawa's (2020) breakthrough design utilizing a transparent gel electrolyte.[21] This electrolyte, comprised of TEMPO-oxidized cellulose nanofibers (TOCN)/ionic liquid/PDMS, exhibits exceptional strain performance (up to 0.22% at ±2 V) due to its unique electrochemical and electromechanical properties. The actuation mechanism leverages an interplay of faradaic capacitor and electrostatic double-layer capacitor (EDLC) effects, with the EDLC effects being predominant. Notably, the study also reveals that the significantly entangled TOCN structure within the electrolyte plays a crucial role in achieving this performance. The fabricated transparent actuator and the corresponding diagram of the TOCN/ionic liquid/PDMS electrolyte layer are presented in Fig. 2(ii).

Phung *et al.* (2020) presented a novel actuator design for tactile displays, achieving significant out-of-plane movement (up to 680 μm) and rapid vibration within a silicone elastomer membrane.[22] This innovative design, as depicted in Fig. 2(iii), employs an integration of double conical dielectric elastomer actuators (DEA) and electrostatic attraction. The critical feature lies in the arrangement of two electrodes with a precisely defined V-structured air gap separating them from the elastomer. Upon application of voltage, the electrodes generate electrostatic attraction forces, causing the elastomer layer to deform significantly and bulge towards the rigid electrode side. This actuation mechanism facilitates the large out-of-plane

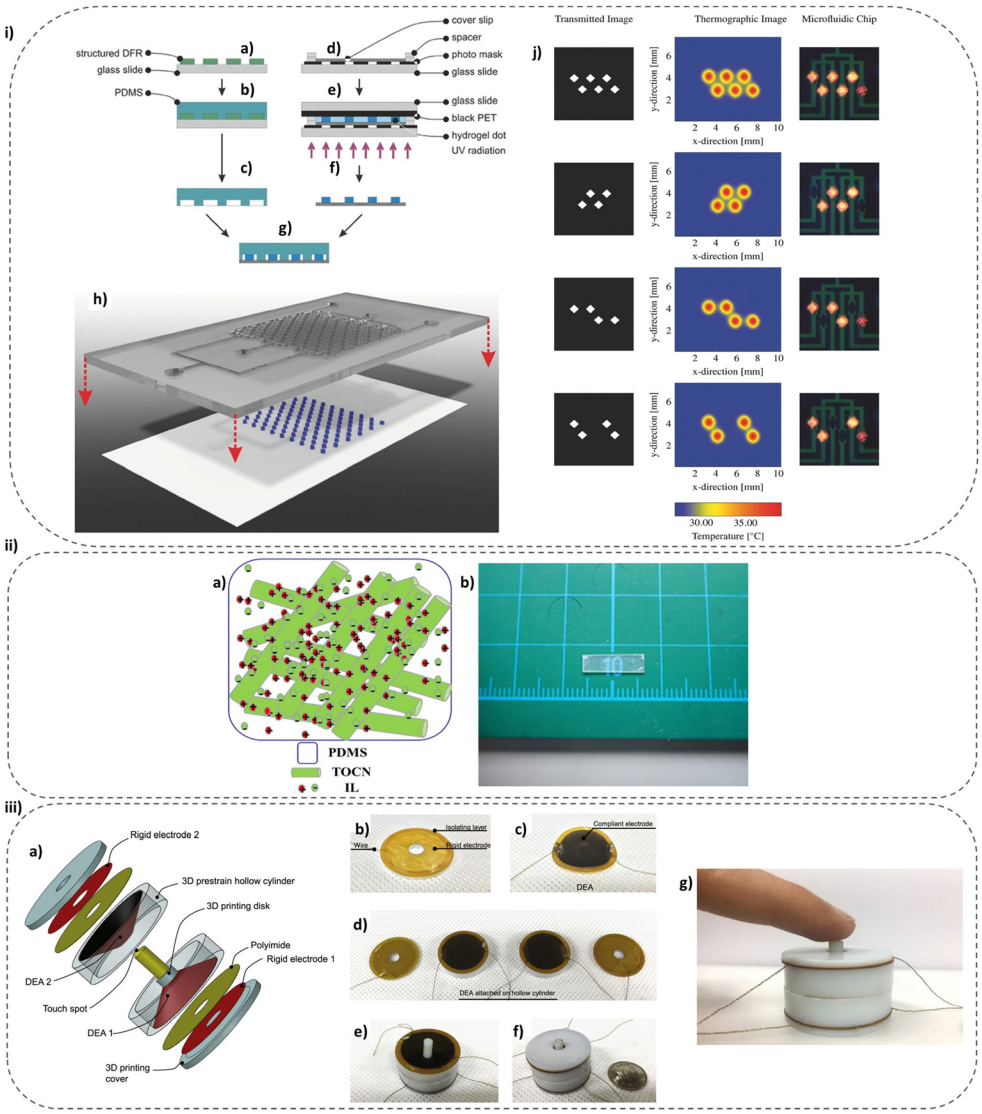

Fig. 2 EAP-based devices: (i) hydrogel microvalve: (a) and (b) to start the fabrication, photolithography with dry film resist (DFR) is used to fabricate a primary mold. (c) PDMS is poured onto the mold, baked, and peeled off. (d) and (e) A polymerization chamber is assembled, filled with solution under inert gas, and exposed to UV light for photopolymerization. (f) and (g) The cover slip with hydrogels and the PDMS chip are plasma-activated, aligned, and bonded. (h) Diagram illustrates the concept of actuator integration with the microfluidic chip. (j) High-integration actuation enables independent control of different hydrogels *via* transmitted image modulation for targeted heating and valve actuation. (ii) Transparent TOCN/ionic liquid/PDMS gel electrolyte actuator: (a) diagram of the layered structure, including the transparent gel electrolyte composed of TOCN, ionic liquid, and PDMS. (b) Realization of the fabricated actuator. (iii) Tactile display: (a) diagram depicting the key components of the tactile display actuator. (b) To start the fabrication process, top and bottom covers are fabricated using a 3D printing process. Subsequently, a highly conductive silver paste electrode is applied to each cover, followed by electrical insulation achieved by a thin polyimide layer (thickness: 50 μm). (c) The DEA is fabricated which comprises a thin layer of dielectric elastomer with adaptable electrodes on each side. When a high voltage (typically several kV) is applied, Maxwell stress is generated across the membrane thickness, causing actuation. (d) The individual components are presented before final assembly. (e) This includes the mounted bottom cover with two integrated DEAs and the designated touch spots. (f) The fully assembled tactile display prototype is showcased. (g) The final fabricated and assembled bidirectional haptic display is presented. (i) Reprinted with permission from ref. 17. Copyright 2017 WILEY-VCH Verlag GmbH & Co. KGaA, Weinheim. (ii) Reprinted (adapted) with permission from ref. 21. Copyright 2020 American Chemical Society. (iii) Reprinted with permission from ref. 22. Minor modifications have been made to figure labels for improved clarity and consistency Copyright 2020 The Author(s), Published by IOP Publishing Ltd. Distributed under a Creative Commons Attribution 4.0 licence https://creativecommons.org/licenses/by/4.0/.

displacements and rapid vibrations observed in the elastomer membrane, suggesting promising advancements for tactile display technologies.

Although different EAP types offer unique advantages and drawbacks, this review places a particular focus on liquid crystal elastomers (LCEs) and their newest addition, ionic liquid crystal elastomers (iLCEs), due to their recent emergence in soft MEMS applications.[23–25] The particular appeal of LCE in MEMS actuators stems from three key factors: tunable actuation direction, tunable mechanical properties, and diverse actuation stimuli. Firstly, the direction of LCE actuation is critically dependent on the orientation of their liquid crystal

molecules (i.e. mesogens). This tunability allows for precise control over the type of mechanical movement achieved,[26,27] ranging from helical bending[28] and radial contraction[14] to even circumferential actuation,[13] mimicking the function of the human eye diaphragm. Secondly, LCE mechanical properties can be readily tuned by altering the rubbery network structure during synthesis and alignment, enabling researchers to fine-tune their performance to achieve desirable characteristics like elastic modulus, strain rates, reflectivity, and birefringence.[29–32] Finally, LCEs can be triggered by diverse stimuli, such as light, heat, electric field, or even humidity, expanding their versatility and broadening their potential applications.[29,33,34] Combined, these properties make LCEs ideal candidates for transduction applications in the MEMS field.

This comprehensive review explores the state-of-the-art of LCE-based MEMS devices, with a specific focus on the methods for integrating these smart soft materials into MEMS. Firstly, the article begins by a foundational explanation of LCEs, including their core component, liquid crystals (LCs). Subsequently, the article explores the preparation of LCEs, encompassing synthesis techniques, as well as the alignment mechanisms. Following the foundational explanation of LCEs, the article delves into the current state-of-the-art MEMS devices that leverage LCE. It provides a comprehensive examination of their application areas, characterization, and the associated fabrication processes. Finally, the article explores cutting-edge methods for integrating LCEs into MEMS using compatible fabrication techniques. Looking towards the future, this review concludes by introducing iLCEs, a novel and enhanced version of LCEs, and highlighting their potential to overcome limitations of conventional LCEs in MEMS applications.

2. Liquid crystals

LCs, the building blocks of LCEs, possess the remarkable ability to exist in mesophases, *i.e.* intermediate states that combine the fluidity of liquids with the ordered structure of crystals.[35] Unlike regular liquids with chaotic molecules, LCs exhibit a degree of long-range order, leading to anisotropic properties in terms of optics, electromagnetism, and mechanics.[35] LCs consist of rod-shaped molecules called mesogens, which self-align in a specific direction.[36] The ability of LCs to maintain structural order in a fluid-like state stems from the self-assembling nature of their constituent mesogens.[37] Furthermore, inherent dipoles in mesogens enable alignment and polarization for LCs.[38] LCs, characterized by reversible transitions between ordered and disordered states, exhibit anisotropic properties in ordered phases due to well-aligned mesogens, whereas disordered phases showcase isotropic behavior due to randomly oriented mesogens.[37,39] The critical temperature at which LCs undergo a phase transition from an isotropic liquid phase to a LC phase is known as the isotropic transition temperature. For nematics, the most common LC phase, the transition temperature is referred to as the nematic–isotropic transition temperature (T_{ni}).[37] Further cooling can lead to another phase transition, from the ordered LC phase to a crystalline solid phase. In the case of nematic LCs, this subsequent transition is referred to as the nematic-crystalline phase transition temperature (T_{nc}).[40] LCs may exhibit two primary ordered phases: nematic and smectic phases, which are discussed in the following.

2.1. Nematic phase

The most prevalent form of ordered LCs is the nematic phase, which features far-reaching orientational order with only local positional arrangement.[35,41] Resembling boats in a canal, the nematic phase features mesogens directed towards the same direction (known as the director ($\vec{n}$), which is a vector representing the average orientation of mesogens in a specific region of the LCs).[37,42] It is named after the Greek word for "thread," reflecting the thread-like structural distortions observed in polarized optical microscopy (POM).[37] The nematic phase of mesogen configuration, characterized by parallel alignment without positional order, is depicted in Fig. 3a.

2.2. Smectic phase

Smectic phases, named after their soap-like structure, exhibit both orientational and positional order.[37,43] Smectic phases display a parallelly layered arrangement with aligned mesogens within each layer, allowing the layers to slide over one another.[37] Smectic A and smectic C are the two most common smectic phases, differing in the orientation of the director.[37] Smectic A phases (see Fig. 3b) feature a layered arrangement with the long axes of the mesogens, aligned normally to the layer (along $\vec{k}$). In contrast, smectic C phases (see Fig. 3c) exhibit a similar layered arrangement, but the long axes of the mesogens are additionally tilted with respect to the layer normal.[42]

3. Liquid crystal elastomers

LCEs, with their unique blend of liquid fluidity and crystalline order, challenge the very foundations of material classifications.[37] Their unique properties have led some researchers to propose their classification as a novel state of matter.[44] LCEs are smart materials that have both the properties of elastomers and LCs. By this combination, LCEs bring together the anisotropic properties of LCs with the entropic elasticity inherent in elastomer networks (see Fig. 4).[45] They are composed of long, flexible polymer chains that are crosslinked to form a network. Within this network are liquid crystal mesogens. As shown in Fig. 5, LCE can be categorized into three main types based on how these mesogens are

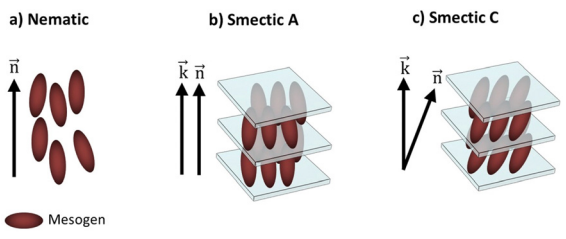

Fig. 3 The three main ordered phases of liquid crystals: (a) nematic, (b) smectic A, and (c) smectic C.

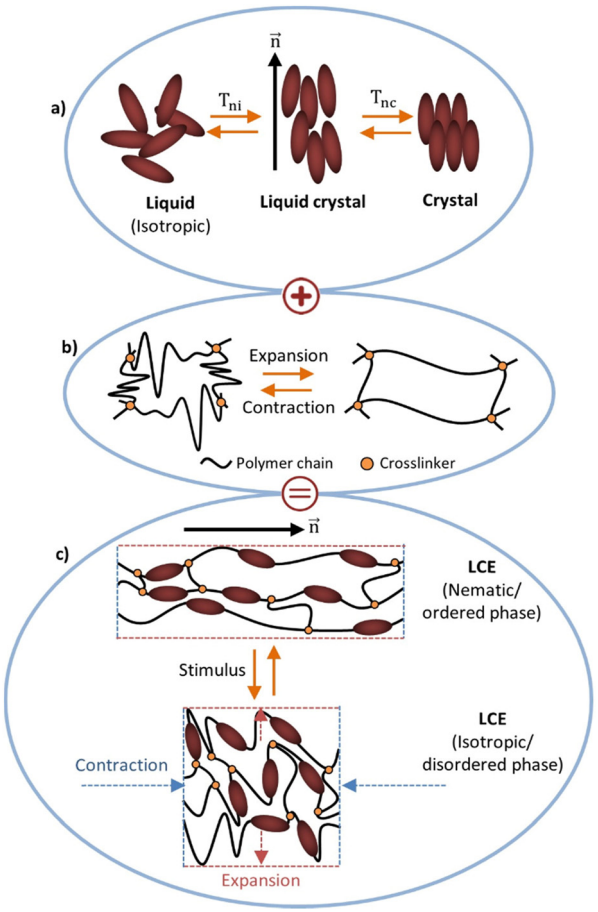

Fig. 4 A schematic of an LCE structure and its actuation principle: LCEs offer a unique material class by merging the order and anisotropy of (a) LCs with the elasticity of (b) elastomers. In LCs, rod-like molecules (mesogens) align along a common direction called the director ($\vec{n}$), defining the nematic (ordered) phase of LCEs. (c) When a stimulus, such as heat, is applied to an aligned LCE in its nematic/ordered phase, the orientation of the LC is disrupted, leading to the actuation mode (isotropic phase) of the LCE.

attached to the polymer chains: main-chain LCE (MCLCE), end-on side-chain LCE (EO-SCLCE), and side-on side-chain LCE (SO-SCLCE).[41] MCLCE have mesogens embedded directly within the polymer backbone, while SCLCE have mesogens attached to the polymer backbone through flexible spacers.[42] SCLCE are subdivided as either end-on, where the mesogen is anchored at its terminus, or side-on, where the mesogen is attached at its center.[42] This arrangement in side-chain groups (loosely crosslinked mesogens in polymer network) provides the greater flexibility and enables the LC molecules to freely rotate and align with the external stimuli. However, the limited coupling between the LC molecules and the polymer backbone can lead to lower mechanical strength and actuation performance compared to MCLCE.[36,46,47] On the other hand, MCLCE incorporate the LC molecules directly into the polymer backbone, forming a more intimate connection between the mesogens and the polymer network.[36,46] This stronger coupling allows for more efficient energy transfer between the LC phase and the polymer network, leading to higher mechanical strength and greater actuation performance (up to 400%[47]). However, MCLCE tends to be less flexible than SCLCE due to the more rigid LC-polymer backbone structure (highly crosslinked mesogens in the polymer network).[47,48]

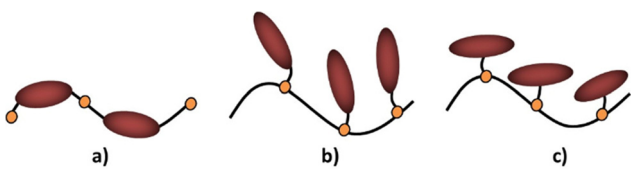

Fig. 5 Molecular configuration of LCE: (a) main-chain LCE, featuring mesogens that are directly integrated into the polymer backbone, (b) end-on side-chain LCE, with mesogens tethered at their end points, and (c) side-on side-chain LCE, where mesogens are connected at their midpoint.

3.1 Preparation of LCE

The synthesis of LCE necessitates two distinct synthetic steps: constructing the LC polymer comprising polymer chains and mesogenic groups, and cross-linking the polymer chains to establish an indefinitely large network.[42] Careful selection of precursor materials and control over reaction conditions are essential for synthesizing LCE with the desired performance characteristics. Table 1 provides examples of LCE precursors, outlining their performance characteristics. While various methods exist for synthesizing LCE, this article focuses on radical polymerization, a prevalent approach employed in LCE-based MEMS research.[25,49] For a comprehensive review of LCE synthesis, readers are referred to the 2012 study by Brommel *et al.*[41]

Radical polymerization is the only practical chemical method to synthesize LCEs from functional monomers such as acrylates and methacrylates.[41] A radical polymerization process starts with a light or heat-activated initiator that breaks apart to form a free electron, which then reacts with the mesogenic polymer chain and crosslinking monomers to achieve total polymerization in a LCE.[37] Owing to the irreversibility of radical polymerization, mesogen alignment, which will be discussed in the following sub-Section 3.3, needs to be induced prior to polymerization and preserved throughout the process, which poses a significant challenge for bulk processing.[37] It is noteworthy that both LCE and liquid crystal networks (LCNs) can be derived from liquid crystal polymers by varying the amount of incorporated crosslinker.[42] In the realm of LCs, the distinction between LCE and LCNs hinges on their respective crosslink densities. These densities, in turn, influence critical factors such as glass transition temperatures (T_g), strain rates, and elastic modulus (E).[49] LCEs typically possess low crosslink densities, whereas LCNs tend to have moderate to high crosslink densities. Consequently, LCNs exhibit higher T_g, lower strain rates, and heightened E compared to LCEs.[29]

3.2 Configuration of mesogens in LCEs

The surface treatment and chosen alignment technique dictate how the mesogens of LCEs are positioned, defining whether they lie parallel (planar) or perpendicular (homeotropic) to the alignment surface (see Fig. 6).[36] The liquid crystal orientation

Table 1 Comparative analysis of selected LCE precursors and their performance characteristics

Example number	LCE/iLCE precursors	Role	Quantity required	Performance	Ref.
1	RM82	Reactive mesogen	RM82 to DMEN (or n-BA) = 1.05 : 1	Bending angle [°] = up to 48 (@25 Hz and @5 kV)	33
	DMEN	Chain extender (first choice)			
	n-BA	Chain extender (alternative choice)	I-651 = 1.5 wt%		
	Irgacure 651 (I-651)	Photo initiator			
2	RM82	Reactive mesogen	RM82 to n-BA = 1.1 : 1	Bending angle [°] = 27.2 ± 11.3 (@180 °C, and @0.05 wt% of chiral dopant)	50
	n-BA	Chain extender	I-651 = 1.5 wt%		
	Irgacure 651 (I-651)	Photo initiator	1.9 mg of R811 per mL of acetone		
	R811	Induce chirality, enabling self-assembly and controlled bending	(0 to 0.2 wt%)		
3	RM257	Reactive mesogen	1 g (1.7 mmol)	(1) Reversible contraction [%] = 34	51
	EDDET	Bifunctional mercaptan	0.1686 g (0.925 mmol)	(2) Actuation force [cN] = 18.7	
	PETMP	Tetrafunctional mercaptan (crosslinker)	0.1466 g (0.3 mmol)	(@0.6 V cm^{-1})	
	HHMP	Photo initiator	0.0265 g (2%)	(3) Lifting 205 times its weight	
4	RM257	Reactive mesogen	95 mol%	Thermal conductivity	52
	PETMP	Crosslinker	5 mol%	= 0.34 W m^{-1} K^{-1}@Homeotropic alignment	
	$C_6H_5COC(CH_3)_2OH$	Photo initiator	0.3 wt%	= 0.22 W m^{-1} K^{-1}@Planar alignment	
5	RM257	Reactive mesogen	1 mmol	Strain [%] = 56–68 self-elongation time [h] ≈ 14	53
	EDDET	Dithiol spacer	0.6 mmol		
	PETMP	Tetra thiol crosslinker	0.2 mmol		
	DCM	Solvent	5 mL		
6	$C_{28}H_{36}O_6$	Reactive mesogen	87 mol%	Deformation [mm] = 2 (actuated by low frequency AC or DC voltages of less than 1 V)	54
	1RM82	Crosslinker	12 mol%		
	Irgacure 651 (I-651)	Photo initiator	1 mol%		
	HMIM-PF6	Ionic liquid	I-651 = 5–35 wt%		

can either be uniform (*e.g.*, planar or homeotropic) throughout the film or exhibit variation across its thickness (*e.g.*, twisted nematic (TN)[55] or splay[56]). In the latter case, TN or splay configurations can occur, where the anchoring command surfaces at opposite ends of the film dictate different alignment preferences for the LC mesogens.[57] In planar alignment, the director aligns parallel to the surface, while in homeotropic alignment, it aligns perpendicular to the surface. In TN alignment, the director rotates gradually throughout the thickness of the film forming a spiral pattern. In splay alignment, the director is spatially undulated throughout the thickness of the film. By controlling the orientation of the director within LCE, researchers can tailor the material's properties (*e.g.* mechanical and optical) to suit specific applications. Highlighting this concept, Rajapaksha *et al.* (2022) employed iLCE as solid electrolytes in organic electrochemical transistors (OECTs).[31] They demonstrated that aligning the director improves both the device's steady-state and transient responses, achieving the highest normalized maximum transconductance (g_m/w = 7 S m^{-1} and 5.5 S m^{-1} for isotropic and planar samples, respectively) among all solid-state organic transistors.[31]

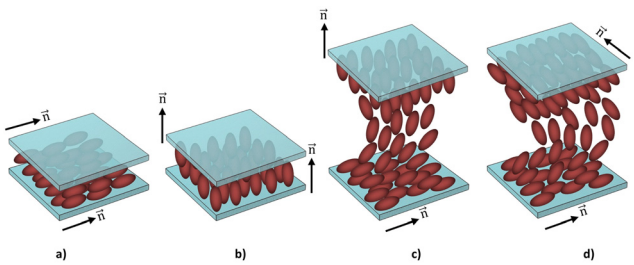

Fig. 6 Various orientations of mesogens in LCEs: (a) planar, where mesogens align parallel to the alignment surfaces, (b) homeotropic, where mesogens align perpendicular to the alignment surfaces, (c) twisted nematic, with a mixture of mesogens aligned both perpendicular and parallel to the alignment surfaces, and (d) splay, where mesogens align parallel to the alignment surfaces but with a 90-degree rotation.

3.3 Alignment methods for LCE

LCE alignment follows the director ($\vec{n}$), as its orientation dictates how the material's molecules are arranged.[58] During alignment, a disordered LCE (polydomain) transforms into a uniformly aligned LCE, known as a monodomain.[59] The alignment of mesogens within LCE materials can be broadly classified into two distinct categories based on their interaction with the alignment method: bulk alignment and interfacial alignment. Bulk alignment methods, like electric field, magnetic field, and mechanical stresses, induce uniform alignment throughout the entire film thickness by applying external fields that interact with the mesogens throughout the LCE film thickness. In electric field alignment, incorporating polar groups (*e.g.*, esters, nitriles, and halogens) into liquid crystal molecules induces their alignment parallel to the applied electric field.[36] When an electric field is applied, the long axes of mesogens will reorient based on their dielectric anisotropy,[38] aligning parallel (positive dielectric anisotropy) or perpendicular (negative dielectric anisotropy) to the field with the degree of deflection depending on the field intensity (see Fig. 7a).[60] In magnetic alignment, due to

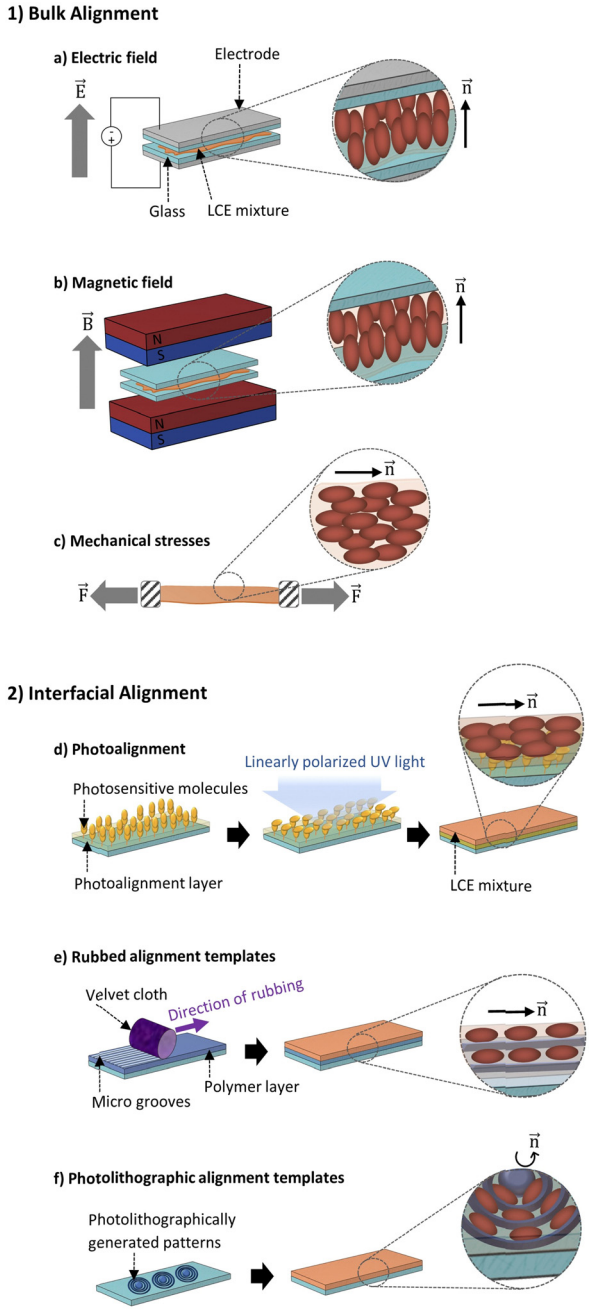

Fig. 7 LCE alignment methods: (1) bulk alignment: (a) electric field: the director aligns with the electric field direction. (b) Magnetic field: mesogens align with the magnetic induction intensity direction. (c) Mechanical stresses: alignment direction follows the stretching direction. (d) Photoalignment: the director can be perpendicular or parallel to the light vector's direction. (2) Interfacial alignment: (e) rubbed alignment templates: the direction of mechanical friction during rubbing defines the alignment direction of the mesogens. (f) Photolithographic alignment templates: microchannel direction dictates the alignment of mesogens within the LCE.

diamagnetic character of mesogens, most mesogens (often with benzene rings) align parallel to the magnetic field (see Fig. 7b),[38,60] while those with cyclohexyl rings (weakly diamagnetic or negative) align perpendicularly.[61] The simplest method for LCE alignment, mechanical stresses,[36] stretches a partially polymerized LCE composition, forcing chain conformations to align with the applied force and lock in place upon full polymerization (see Fig. 7c).[37] On the other hand, interfacial alignment methods focus on the LCE film's surface, manipulating the interaction between the LCE and neighbouring layers. Common approaches include photoalignment, and pre-designed alignment templates created by rubbing or photolithography. Photoalignment method involves treating substrates with light, enabling them to control the orientation of LCs.[62] In this method, a photosensitive layer on the substrate undergoes light-induced reorientation of its molecules (or fragments) and their photoproducts, creating an anisotropic interface that dictates the preferred alignment direction for mesogens (see Fig. 7d).[62]

This method leverages exposure time as a control parameter for the alignment direction of mesogens within the material.[62] By precisely modulating the exposure duration (short *vs.* long), the alignment of mesogens can be tailored to achieve either a parallel or perpendicular orientation relative to the alignment surface.[63–65] The alignment templates contains surface patterns with topologically trapped structures that confine mesogens at the surfaces (see Fig. 7e and f).[36,66] These surface alignment coatings are also known as command layers,[67] as they enforce mesogens' alignment. Fig. 7e depicts parallel alignment of the mesogens with the rubbing direction.[42] Conversely, Fig. 7f shows a circular alignment of the mesogens, following the direction of the pre-designed microchannel patterns on the glass substrate.[68] In contrast to photoalignment, which can influence the orientation of LCs throughout the entire polymer film, rubbing treatment primarily affects the topmost surface layer.[62] Fig. 7 showcases diverse alignment methods for LCE, each offering specific advantages and drawbacks, as detailed in Table 2. The choice of method will depend on the specific target application. This capability for precise alignment gives LCE the following unique properties. (i) Shape memory: LCE can undergo large, reversible shape changes in response to external stimuli such as light,[69] heat,[70] and electric field.[42,71] This is due to the fact that the orientation of the liquid crystal molecules can be altered by these stimuli, which in turn changes the elastic properties of the material.[36] (ii) Anisotropy: unaligned LCE exhibit isotropy, where randomly oriented mesogens average out their properties in all directions. Conversely, alignment induces anisotropy, causing the long axes of mesogens to point in a preferred direction. This results in a material with directionally dependent mechanical and optical properties.[37] (iii) Low hysteresis: LCE exhibit low hysteresis,[72,73] recovering their original shape quickly and efficiently after being deformed. Thisis an important property for applications where the material needs to be able to frequently transition between different shapes.[69,74] The exploration of novel alignment techniques remains an active area of research, promising even greater control over LCE properties.

4. LCE MEMS state-of-the-art

Notable LCE-based MEMS devices have been demonstrated using various implementation strategies, as summarized in

Table 2 Advantages and disadvantages of the different alignment methods for LCE

Alignment method	Advantages	Disadvantages
Electric field[37]	Multi-orientable	Requires specific reaction chemistries and large fields
Magnetic field[15,37,75]	Homogeneous through-thickness alignment	High-intensity fields (1.2 T and 11 T), extended-duration (12 hours to 3 days)
Mechanical stresses[76–79]	Simple and effective process	Limited scalability, non-programmable, fracture stress
Photoalignment[37,49,80,81]	Capability to create complex patterns (*e.g.* radial and azimuthal), complex-substrate compatibility	Specialized equipment required, wavelength restriction ($\lambda > 400$ nm), high-field inaccessibility, requires specific photosensitive materials
Rubbed alignment templates[36]	Robust and scalable, industrial-scale applicability	Accumulation of static electricity, generation of fine particulate matter
Photolithographic alignment templates[68]	High-yield, versatile, dimensional and geometric control	Photolithographic resolution limit, not readily scalable

Table 3. It is noteworthy that due to the viscoelastic nature of LCEs, creep deformation is a common phenomenon observed in these LCE-based MEMS actuators (see Table 3). Creep time, the gradual deformation of an actuator under constant load, is an important factor to consider when designing and operating LCE-based MEMS.

The idea of incorporating LCEs into MEMS was first presented by Brundel *et al.* in 2004.[91] Their work demonstrated the feasibility of LCE integration using standard MEMS fabrication techniques. This pioneering research established the foundation for two primary LCE integration methods: monolithic integration, where the LCE is directly manufactured on the wafer alongside other MEMS components, and hybrid assembly, where pre-fabricated LCE films are bonded to existing MEMS structures. Following the idea, Buguin *et al.* (2006) introduced a novel approach for the fabrication of microscale actuators utilizing LCEs.[82] This method leverages replica molding, a soft lithography technique, to create micro patterned molds that are subsequently used to define the shape of a light-curable LCE material. These LCE micropillars exhibit a significant thermal response, reversibly contracting by 30–40% upon heating, as illustrated in Fig. 8(i). Sánchez-Ferrer *et al.* (2009) developed the first microgripper actuated by an LCE film that utilizes thermally induced shape changes in an LCE film, enabling controlled manipulation of objects.[15] Fig. 8(ii) provides a schematic illustration of the device alongside an image of the fabricated microgripper, highlighting the application of LCE actuation for micromanipulation tasks. The LCE film exhibits actuation stress reaching 60 kPa and deformation strain up to 150% under applied electric voltage between 1.5 V and 3.5 V. Sánchez-Ferrer *et al.* (2011) further explored LCE actuation by introducing a microfluidic valve.[83] This innovative design utilizes the same thermal actuation principle but cleverly exploits the expansion and bending of LCE to control fluid flow. Due to the nematic-to-isotropic phase transition, which serves as the actuation mode of LCEs, the LCE film effectively opens and closes the microfluidic channel. The microvalve design integrates a compressed LCE film (50 N) between microfluidic channels. This configuration leverages water flow (271 $\mu L\ s^{-1}$) and a maximum heating power of 11 W to perform actuation. Fig. 8(iii) presents both a schematic illustration and a fabricated image of the microvalve. In 2014, inspired by the human eye, a novel thermally-actuated LCE iris with radial motion is introduced by Schuhladen *et al.*[14] The design leverages integrated heaters and a custom magnetic field for actuation control. Notably, the iris exhibits repeatable actuation and controllable contraction, fabricated by molding LCE with embedded heaters. While boasting a 10–90% diameter variation, unequal heating/cooling areas lead to a faster closing time (3 s) compared to opening (7 s). Fig. 8(iv) illustrates the fabricated LCE-based iris.

Recent research in 2019 has explored the use of LCE for fabricating soft tubular actuators.[84] These actuators exhibit impressive multi-directional actuation capabilities, enabling bending, expansion, and homogenous contraction of up to 40%. Furthermore, they demonstrate a high maximum work density of 150 kJ m^{-3} under a moderate applied stress of 0.31 MPa. A significant advantage of this actuation method lies in its low voltage control requirement (1–3 V), facilitating straightforward integration and operation. Fig. 9(i) presents a schematic diagram detailing the fabrication process of the tubular actuator, highlighting its internal architecture with three embedded heating wire sets. Selective activation of these heating wire sets allows for controlled bending of the actuator in various directions. Highlighting a novel advancement in LCEs, He *et al.* (2020) introduced self-healing LCE actuators.[85] Their design leverages a layered manufacturing process enabled by dynamic bond exchange reactions. This approach utilizes fluid flow through microchannels within the LCE to induce actuation through heating and cooling effects. Crucially, incorporating dynamic covalent bonds, *e.g.* disulfides, into the LCE network imbues these actuators with self-healing capabilities (Fig. 9(ii)). This translates to reprogrammability, reconfigurability, recyclability, and reusability, achieved through a heating mechanism. The fabrication process involves laser-cutting a microfluidic channel within a 1 mm thick LCE sheet. This patterned sheet is then sandwiched between two solid 0.3 mm LCE layers. The entire assembly is then heated to 180 °C under pressure for 1 hour, allowing dynamic bond exchange reactions to permanently integrate the layers. Finally, the structure is cooled, stretched by a factor of two, and held for 24 hours to align the internal mesogens for optimal actuation. This meticulous process results in a robust, self-healing LCE actuator with a microfluidic channel for fluid-driven actuation.

In a recent study by Choi *et al.* (2023), a novel design for soft actuators using electroactive LCE (e-LCE) was introduced.[33] This approach utilizes electrostatic forces to achieve rapid actuation speeds of around 25 Hz. Unlike traditional dielectric

Table 3 Comparative properties of recently developed LCE-based MEMS devices

Actuation mechanism	Electrode type	Actuation quantity [unit]	Output [unit]	Creep time	Dimensions of LCE	Method for integrating LCE	Application	Year	Ref.
Thermal	Heating stage	Temperature [°C] = 100–130	Contraction [%] = 30–40	Not provided	Diameter [μm] = 20 Height [μm] = 100	Molding	Micro-pillar	2006	82
Electrostatic	Gold wires	Voltage [V] = 1.5–3.5	Strain [%] = up to 150	Not provided	Volume [mm^3] = 16 × 4 × 0.03	Adhesion by oxygen plasma activation	Microgripper	2009	15
Electro-thermal	Copper	P_{heat} [W] = 11	f_{switch} [Hz] = 0.01	Not provided	Volume [mm^3] = 10 × 10 × 1.04	Compressing the LCE between two parts by 50 N	Micro-valve	2011	83
Electro-thermal	Platinum wires-based integrated heaters	Voltage [V] = 50	Diameter change [%] = 10–90	3–7 s	Diameter [mm] = 12 Thickness [mm] = ∼0.3	Molding	Tunable iris	2014	14
Electro-thermal	Copper wires	Voltage [V] = ∼3	Contraction [%] = ∼40	30 s	Volume [mm^3] = 39 × 30 × 1	Molding	Tubular actuator	2019	84
Hot/cold fluid (by two gear pumps)	Not applicable	Temperature [°C] = 90 and 20	Strain [%] = 30@0.25 Hz = 10%@1Hz	∼3 s	Area [mm^2] = 25 × 16, and = 38 × 20	Laser-cut LCE channel sandwiched by two LCE sheets	Fluid-driven actuator	2020	85
Electrostatic	Copper: contact electrode aluminum: non-contact electrode	Voltage [kV] = 5	Bending [°] = ∼65 (for a 25 μm-thick LCE)	∼25 Hz	Volume [mm^3] = 10 × 0.5 × 0.025	Cell filling using two glass slides	Soft actuator	2023	33
Electrostatic	Copper foil	Voltage [V] = 150	Strain [%] = 30	∼60 s	Volume [mm^3] = 26 × 8 × 0.8	Molding	Self-sensing actuator	2023	86
Photo-thermal	Not applicable	Temperature [°C] = 20–120 Light [nm, W] = 808, 1	Displacement [mm] = up to 200 (5.6 mm s^{-1})	∼1 s	Volume [mm^3] = 45 × 4 × 1	Molding	Soft scrolling actuator	2024	87
Electro-thermal	Chromium/copper	Voltage [V] = 17.5	Tip displacement [mm] = ∼2 mm	Not provided	Not provided	Molding	Self-sensing actuator	2024	88
Electro/Photo-thermal	Silver (Ag FDs)	Voltage [V] = 3 Current [mA] = 200	mBending [°] = 102° (for a 1 mm-thick LCE)	∼40 s	Not provided	Molding	Self-sensing actuator	2024	89
Electro-thermal	CNT and graphite microparticles	Voltage [V] = 12	Sensing current [mA] = 12 to 15	6 s	Volume [mm^3] = 5 × 1 × 0.5	Molding	Self-sensing actuator	2024	90

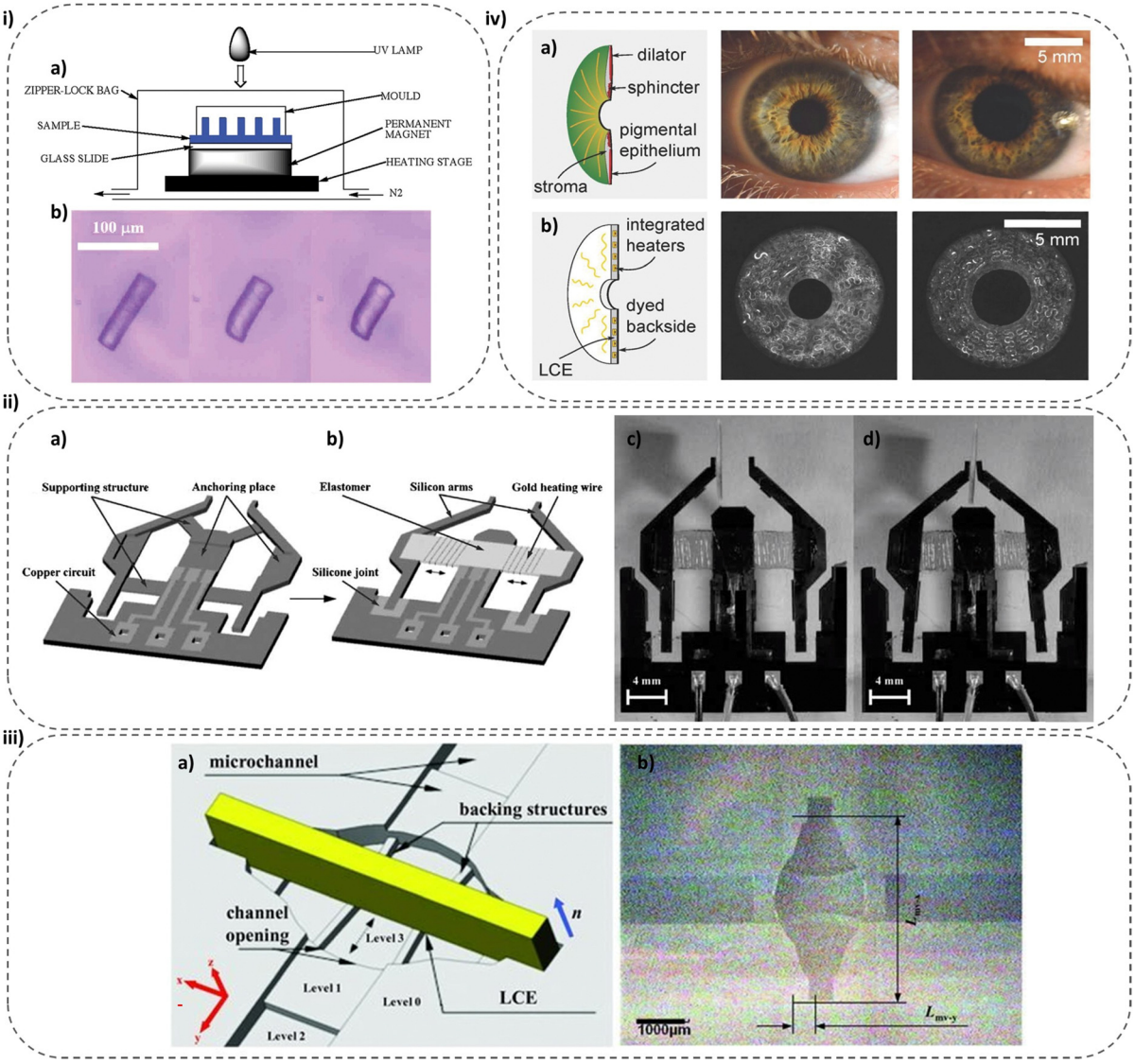

Fig. 8 LCE-based microdevices: (i) responsive LCE micropillars: (a) fabrication setup for LCE micropillars. (b) Thermally induced contraction (35% along major axis) of a heated pillar (the temperatures progress from left to right: 100 °C, 120 °C, and 130 °C). (ii) LCE microgripper: (a) the silicon carrier used for batch production and (b) the elastomer mounted on the completed gripper mechanism. (c) Open and (d) closed states achieved by applying electrical power. The nematic-to-isotropic phase transition in the LCE film induces dimensional changes, enabling gripping functionality. (iii) LCE microvalve: (a) schematic representation of a half microvalve. (b) Pre-fabricated microfluidic components before final assembly. (iv) Tunable LCE iris: (a) human iris schematic shows the sphincter and dilator muscles responsible for pupil constriction and dilation, respectively. (b) LCE iris with integrated heaters mimics human iris function through contraction and expansion upon electrical heating. (i) Reprinted (adapted) with permission from ref. 82 Copyright 2006 American Chemical Society. (ii) Reprinted with permission from ref. 15. Copyright 2009 WILEY-VCH Verlag GmbH & Co. KGaA, Weinheim. (iii) Reprinted with permission from ref. 83. Copyright 2011 WILEY-VCH Verlag GmbH & Co. KGaA, Weinheim. (iv) Reprinted with permission from ref. 14. Copyright 2014 WILEY-VCH Verlag GmbH & Co. KGaA, Weinheim.

elastomer actuators where the LCE film is sandwiched between two electrodes, this design employs a unique configuration with the e-LCE film physically separated from one electrode. This separation grants the e-LCE film a high degree of freedom for bending and deformation during actuation. The fabrication process involves a cell filling technique. Two glass slides are spin-coated with an Elvamide solution and then rubbed with a velvet cloth to achieve a uniform alignment. These rubbed slides are then assembled in an anti-parallel configuration with a 50 μm spacer separating them. This cell is filled with the LCE precursor mixture, followed by crosslinking and film release from the glass slides. Finally, one copper electrode is attached to one surface of the e-LCE film, while the other aluminum electrode remains separate. By applying an electric potential of approximately 5 kV to the electrodes, the researchers achieved a maximum bending angle of around 65° for a 25 μm thick LCE film with a length and width of 10 mm and 0.5 mm, respectively. Fig. 9(iii) comprehensively depicts the actuator's operational principle, its corresponding electrical equivalent circuit, and the film's deformation response upon voltage application.

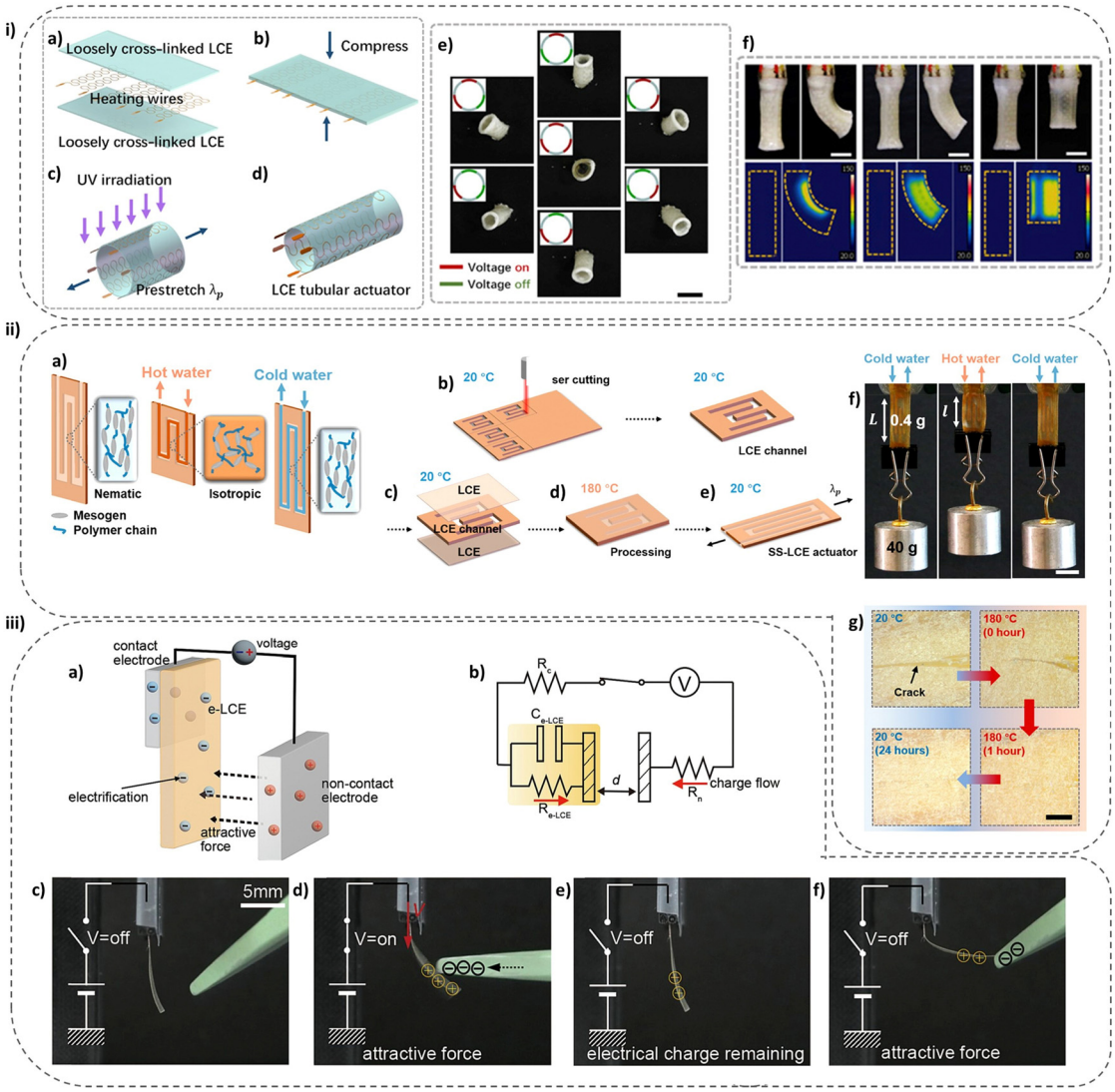

Fig. 9 LCE-based actuators: (i) tubular LCE actuator: (a) first, three serpentine heating wires are sandwiched between two loosely cross-linked LCE films. (b) The layered structure is compressed slightly for enhanced adhesion. (c) The thin film is rolled into a tube shape. (d) The LCE tube is stretched and exposed to UV light to complete the actuator. (e) The measured contraction profile of the LCE actuator upon activation with all three heating wires (solid line: theoretical prediction, dots: experimental results) are plotted. (f) Real and thermal images of the actuator during actuation, demonstrating bending motion with one or two heating wires activated and homogeneous contraction with all three activated are demonstrated (scale bars (e) and (f): 1 cm). (ii) Fluid-driven LCE actuator: (a) schematic diagram depicting the actuator's response to hot water injection into its internal microfluidic channel. The hot water induces a nematic-to-isotropic phase transition in the LCE, resulting in significant contraction. Conversely, cooling the water within the channel promotes the reverse transition (isotropic-to-nematic) and restores the actuator to its initial configuration. (b) To start the fabrication process, a laser cutter is employed to create a microfluidic channel within a 1 mm thick LCE sheet. (c) The channelled LCE sheet is sandwiched between two solid LCE thin film layers, each possessing a thickness of 0.3 mm. (d) The layered structure undergoes heating to 180 °C under a compressive force of 1 N for 1 hour, facilitating a dynamic exchange reaction that firmly bonds the three LCE layers into a single, integrated unit. (e) The structure is cooled to 20 °C and then stretched by a factor of two for 24 hours to achieve optimal alignment of the mesogens within the LCE. This final step yields the functional fluid-driven LCE actuator. (f) Depiction of the completed LCE actuator alongside a visual representation of its reversible fluid-driven actuation mechanism. (g) Illustration of the repair process for an open crack in the LCE film, showcasing its inherent self-healing capability in different stages. (iii) Electroactive LCE actuator: (a) electrostatic actuation mechanism schematic of an e-LCE and (b) the associated equivalent circuit. The incorporation of dimethylethylenediamine (DMEN) facilitates the migration of injected charge within the e-LCE from the electrode in contact. This creates a voltage difference with reference to the distant electrode, leading to electrostatic attraction. The resistances of the contact electrode (R_c), distant electrode (R_n), and e-LCE ($R_{e\text{-}LCE}$) are represented, along with the distance ("d") between the e-LCE and the distant electrode. (c)–(f) These panels illustrate the e-LCE's actuation under different voltage applications. When a voltage is applied to the electrode in contact, the e-LCE gains a charge of identical polarity. This induces an opposite charge on the counterpart electrode, effectively creating an air gap capacitor. Consequently, an attractive force arises between the e-LCE and the distant electrode. Even after removing the voltage, the e-LCE retains its charged state, and the electrostatic force persists. The changing quantity of surface charges depicted in these panels represent the relative magnitudes of the electrostatic interactions across varying operational settings. (i) Reprinted with permission from ref. 84. Copyright 2019, The Authors, published by American Association for the Advancement of Science (AAAS). Reprinted/adapted from ref. 84 © The Authors, some rights reserved; exclusive licensee American Association for the Advancement of Science. Distributed under a Creative Commons Attribution Non Commercial License 4.0 (CC BY-NC) https://creativecommons.org/licenses/by-nc/4.0/. (ii) Reprinted (adapted) with permission from ref. 85. Copyright 2020 American Chemical Society. (iii) Reprinted (adapted) with permission from ref. 33. Copyright 2023 Elsevier B. V. All rights reserved.

This method successfully produced various functional actuators like pop-up letters, Kirigami springs, and flapping beetle wings, highlighting its potential for studying electric field-driven soft actuator mechanics.

The field of self-sensing actuators has seen significant growth, with a diverse range of designs emerging.[92] In a notable development for LCE-based electronics, Zheng *et al.* (2024) presented a cost-effective fabrication method using screen printing to develop a self-sensing LCE actuator, which is shown in Fig. 10(i).[89] This approach enables the creation of multi-functional devices by printing three functional layers onto a thermo-responsive LCE film. The first layer comprises CB for converting absorbed near-infrared (NIR) light into heat. The second layer utilizes silver fractal dendrites (Ag FDs) to achieve

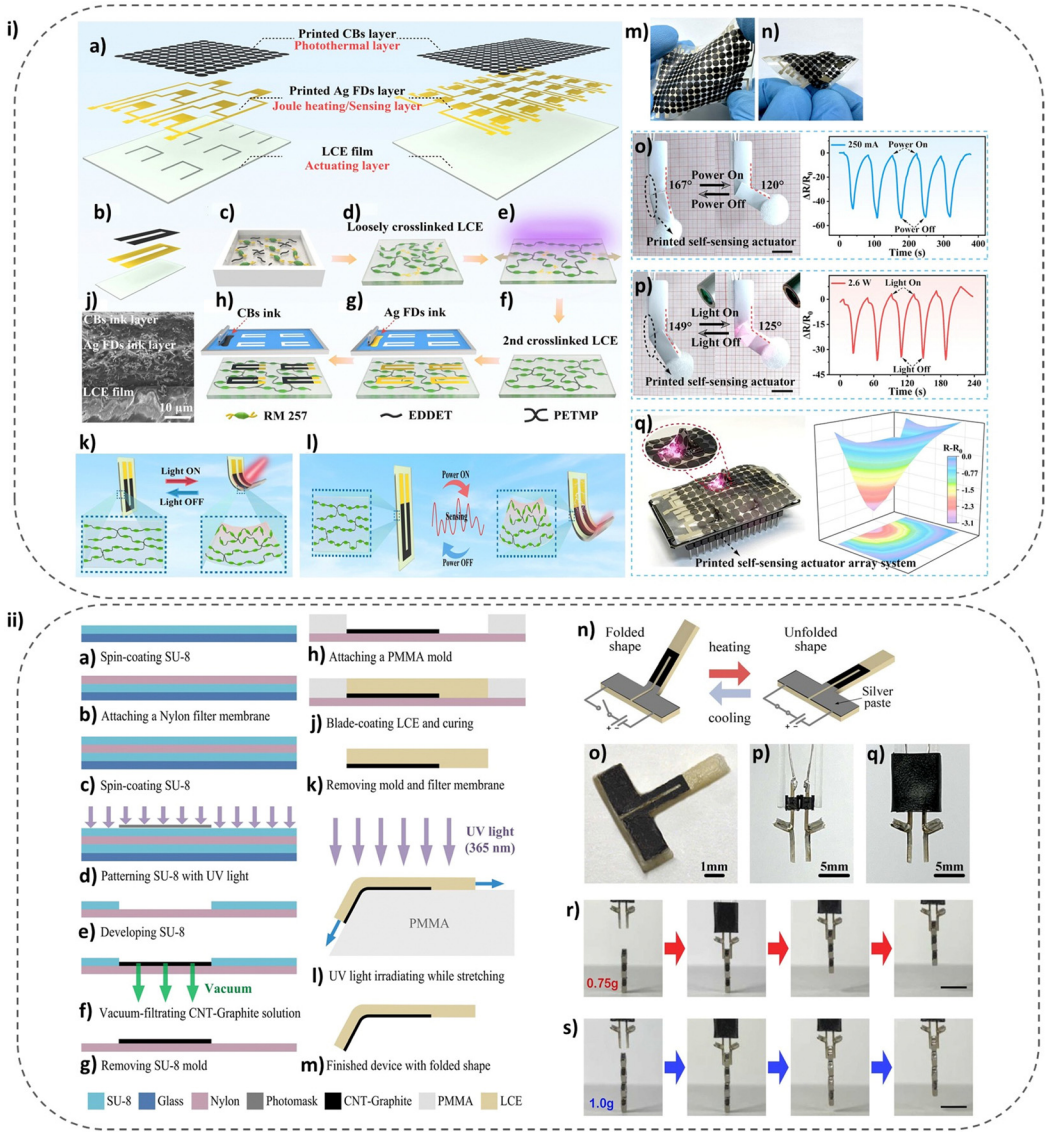

Fig. 10 LCE-based actuators: (i) self-sensing LCE actuator: (a) schematic illustrations of the LCE-based printed self-sensing actuator matrix and LCE-based printed NIR light sensing matrix configuration. (b)–(h) Graphical representations of the fabrication process. (j) Scanning electron microscope (SEM) cross-section of a printed LCE-based self-sensing actuator. (k) and (l) Operational principles of the LCE-based printed self-sensing actuator when subjected to NIR and electrical stimuli, respectively. (m) and (n) Photographs of the fabricated LCE-based printed NIR light sensing matrix configuration and LCE-based printed self-sensing actuator matrix configuration, respectively. (o) and (p) Photographs and corresponding sensor test results demonstrating the application of the LCE-based self-sensing actuator to control a robotic arm in response to electrical and NIR light stimuli, respectively (scale bar represents 15 millimeters). (q) Image and corresponding 3D map depicting the response of the LCE array system to laser irradiation. (ii) Self-sensing LCE-based low power actuator: (a)–(m) sequential illustrations depict the fabrication process of the miniaturized electrothermally driven soft actuator. (n) Schematic representation of the actuator's operational principles. (o) Photograph of the fabricated miniaturized actuator. (p) Photograph of the assembled two-finger gripper. (q) Photograph of the two-finger gripper with a protective heat shrink tubing enclosure. (r) and (s) Snapshots illustrate the gripper's actuation sequence for grasping two distinct weights: 1 g and 0.75 g (scale bar: 10 mm). (i) Reprinted with permission from ref. 89. Copyright 2024 Elsevier B. V. All rights are reserved, including those for text and data mining, AI training, and similar technologies. (ii) Reprinted (adapted) with permission from ref. 90. Copyright 2024 Published by Elsevier B. V.

both Joule heating upon electrical stimulation and strain sensing capabilities. Finally, the underlying LCE film serves as the actuation element, shrinking in response to heat. They explored the impact of LCE film thickness on actuation, finding a decrease in bending angles with thicker films (maximum bending angles of 42°, 82°, and 102° at 64 °C, 81 °C, and 91 °C, respectively). Notably, the LCE devices exhibited self-sensing behavior linked to bending, with maximum resistance changes of −12.6%, −36.3%, and −55.0%, respectively. By strategically customizing the printing patterns, the authors successfully fabricated a diverse range of LCE devices. These include single self-sensing actuators that respond to either electrical or NIR light stimulation, NIR light sensors capable of detecting light intensity, position, and size, and even integrated arrays combining actuator and sensor functionalities. The fabricated LCE devices demonstrate exceptional actuation performance, good cycle stability, and accurate self-sensing. Notably, the NIR light sensing functionality holds significant promise for applications in unmanned aerial vehicle (UAV) flight safety systems.

Bypassing limitations of temperature-dependent sensors in soft robotics, Chi *et al.* (2024) introduced a miniaturized soft actuator with a unique combination of high force and deformation generation, alongside self-sensing capabilities that are remarkably independent of temperature variations (see Fig. 10(ii)).[90] This innovative design integrates a molded LCE layer for actuation with a conductive composite layer (CCL) containing CNT (carbon nanotube) and graphite microparticles. The CCL serves a dual function: electrothermally heating the LCE layer and enabling piezoresistive strain sensing due to its changing electrical resistance under deformation. Notably, the authors address the challenge of temperature-induced errors in strain sensing by meticulously controlling the CNT-to-graphite ratio within the CCL. By exploiting their opposing temperature coefficients of resistance, a near-zero TCR (temperature coefficient of resistance) is achieved for the CCL. This optimization allows the CCL to function as a highly accurate strain sensor, offering self-sensing capabilities that are remarkably independent of temperature variations. Furthermore, the design facilitates simultaneous actuation and sensing through the same electrical terminals, while the device's compact size contributes to low actuation voltage and fast response time. The reported performance characteristics include an initial CCL resistance of 1.05 kΩ, changing to 820 Ω upon actuation (corresponding to a current range of 12–15 mA). Finally, they validated the functionality by constructing a two-finger gripper that leverages the self-sensing CCLs to estimate the weight of grasped objects. This work presents a significant leap forward for miniaturized soft actuators with potential applications in diverse fields requiring precise control and temperature-insensitive feedback.

In a significant advancement for physical rehabilitation applications, Min *et al.* (2023) have developed a novel self-sensing LCE actuator fabricated within a polytetrafluoroethylene (PTFE) mold.[86] The key innovation lies in incorporating conductive materials, specifically carbon black (CB) and graphite, during a two-step fabrication process (see Fig. 11(i)). First, conductive CB and graphite particles are dispersed throughout the LCE mixture during cross-linking, ensuring uniform distribution and optimal alignment of the mesogens. Subsequently, the LCE film is coated with an additional thin layer of conductive CB and graphite on its surfaces *via* immersion in a toluene dispersion. This two-step approach is crucial for achieving LCE with high and stable electrical conductivity throughout actuation cycles. The resulting LCE itself functions as both actuator and sensor. When a voltage is applied, Joule heating from the dispersed and surface-coated conductive materials disrupts the mesogens, triggering a nematic-to-isotropic phase transition. This transition manifests as a contraction along the initial alignment axis and an expansion perpendicularly, generating the desired actuation. The self-sensing functionality is inherently coupled. As the LCE deforms during actuation, the distribution and geometry of the conductive network within the LCE matrix changes, altering the overall electrical resistance. By monitoring this resistance change, the LCE can essentially sense its own deformation in real-time, eliminating the need for additional external sensors.

Liang *et al.* (2024) introduced a novel soft actuator design which is an MXene-doped LCE actuator with a twisted, Rotini-like structure (see Fig. 11(ii)).[87] This actuator achieves coordinated dual-mode actuation *via* heat/cooling or near-infrared light due to MXene's photothermal effect. This surpasses traditional single-mode actuation, offering greater control than traditional single-mode actuation. The fabrication process incorporates MXene into the LCE solvent, followed by cross-linking, uniaxial stretching, and a final coaxial twist to create the Rotini-like geometry. This geometry enables autonomous rolling due to local snapping motions. The dual-mode actuation offers independent activation by heat or light, ensuring stable operation under various conditions. Additionally, the interplay between these modes allows for complex maneuvers, like braking during autonomous rolling with strategic heat and light application. The MXene-doped LCE's high-temperature resistance expands its applicability. This research holds significant promise for the future of soft robotics, paving the way for more sophisticated actuators.

In a novel approach by Lo *et al.* (2024), a self-sensing soft actuator achieved bi-stability by leveraging the interplay between a thermo-responsive LCE cantilever and the shape memory effect of a CNT-dispersed ionogel finger.[88] The actuator utilizes a micromachined heater layer to control a thermo-responsive LCE cantilever, which bends the finger. The ionogel finger then retains this bent shape due to its shape memory effect, achieving bi-stability without constant power consumption. Additionally, the ionogel finger's electrical resistance allows the actuator to self-sense its position. As illustrated in Fig. 11(iii), this design integrates these components to enable bi-stable operation without continuous power input. The fabrication process involves micromachining the heater layer with a thin-film chromium and copper layer on a glass substrate. The LCE cantilever is cured from a prepolymer under UV light, while the ionogel finger is prepared by mixing solutions and CNT particles, then cured in a mold with UV light. Finally, all three components are assembled onto a base using a PDMS

adhesive. The authors also explore the feasibility of a gripper by assembling two such actuators.

Expanding the potential of LCEs beyond traditional actuation and sensing applications, Li *et al.* (2012) demonstrated their utility in energy harvesting (see Fig. 12(i)).[93] Specifically, they developed LCE-based actuators for artificial heliotropism in solar cells. These actuators, composed of fiber networks, single-wall CNTs, and LCEs, can be directly driven by sunlight, eliminating the need for external power sources for solar tracking. When exposed to sunlight, these actuators contract,

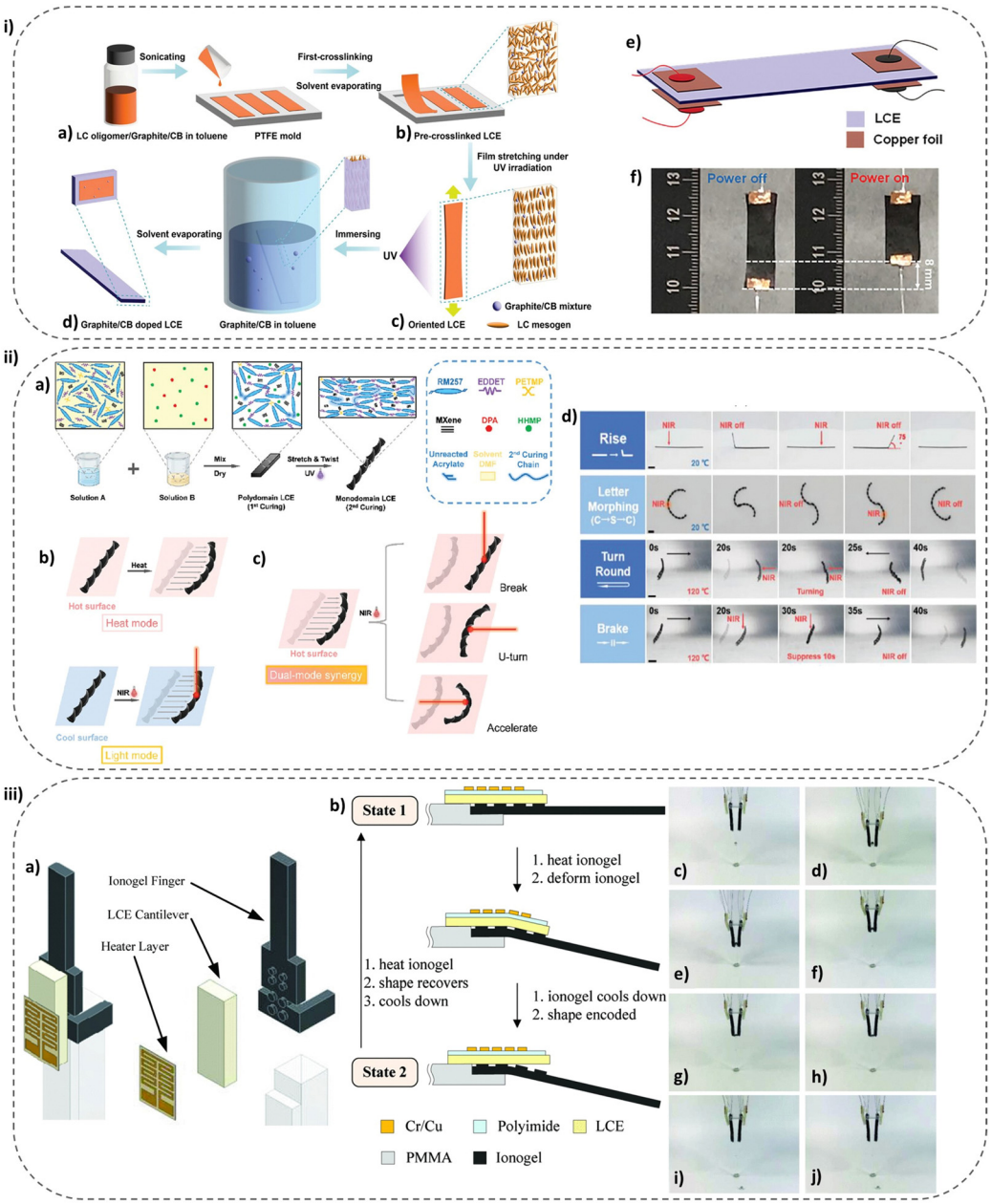

Fig. 11 LCE-based actuators: (i) self-sensing graphite/CB dopped LCE actuator: (a) to start the fabrication process, a mixture of liquid crystal oligomer, graphite, and CB is prepared in toluene. (b) The LCE undergoes a pre-crosslinking step. (c) The LCE is aligned with a parallel orientation of mesogens. (d) The aligned LCE is doped with graphite or CB. (e) A schematic depicts the graphite/CB doped LCE actuator utilizing copper foil electrodes. (f) Depicts a photograph of the LCE actuator in its off and on states. (ii) MXene-doped LCE actuator: (a) a schematic diagram illustrates the steps involved in fabricating the MXene-doped LCE actuator. (b) This actuator exhibits a dual-mode actuation mechanism responsive to both heat and light individually. (c) MXene doping empowers the actuator with the ability to respond simultaneously to both heat and light stimuli. (d) Programmable actuation of different MXene-doped LCE actuators is depicted here, with all measurements performed at a light intensity of 1 W cm^{-2}. (iii) Self-sensing soft actuator with thermo-responsive LCE cantilever: (a) schematic diagram of the bi-stable actuator. (b) Schematic illustration of the operational principle for achieving bi-stability. (c) Snapshot images demonstrating the bi-stable gripper grasping and releasing an object. (i) Reprinted with permission from ref. 86. Copyright 2023 The Authors. Advanced Sensor Research published by Wiley-VCH GmbH. (ii) Reprinted (adapted) with permission from ref. 87. Copyright 2023 2023 Wiley-VCH GmbH. (iii) Reprinted (adapted) with permission from ref. 88. Copyright 2024, IEEE.

tilting the solar cells towards the sun. This innovative approach resulted in a substantial increase in photocurrent, reaching up to 3700%. PTFE molding was employed to fabricate the device.

Harnessing the potential of LCEs for energy harvesting, Wang *et al.* (2022) developed a LCE twist fiber (LCETF) with a fixed twisting alignment of mesogens (see Fig. 12(ii)).[94] This LCETF exhibits untethered and reversible responsiveness, demonstrating exceptional rotational performance when triggered by heat. Leveraging the LCE material's significant contractile ratio, the LCETF can achieve a rotational deformation of up to 243.6° mm^{-1}. Notably, the specific torque generated by the LCETF reaches 10.1 N m kg^{-1}, surpassing previous records. The LCETF's capabilities can be harnessed in a rotating microengine to convert heat into electricity, producing an induction voltage as high as 9.4 V.

5. Manufacturing of LCE using MEMS-compatible techniques

Conventional methods for fabricating LCE often rely on mechanical procedures that limit their scalability and consistency. These methods, such as molding,[14,18,84] 3D printing,[20,95] and capillary filling,[96,97] often involve a high degree of human intervention and can produce variations in alignment and morphology. For instance, molding and cell filling processes, requiring manual peeling and cutting for final shapes, hinder integration with MEMS devices due to a lack of precise patterning.[49] To address these limitations, researchers have explored MEMS-compatible fabrication techniques that offer greater precision, reproducibility, and suitability for large-scale production. Until now, two MEMS-compatible fabrication methods have been proposed for developing LCE structures: multi-layer spin-coating and maskless selective polymerization.

5.1 Multi-layer spin coating method

Ditter *et al.* (2017) proposed a MEMS-compatible fabrication process for integrating LCEs into MEMS.[23] This method involves spin-coating a multi-layer structure onto a substrate, followed by photolithography and etching to create patterned LCE films.[23] To avoid LCE swelling caused by conventional photoresist developers, this method utilizes fluorinated

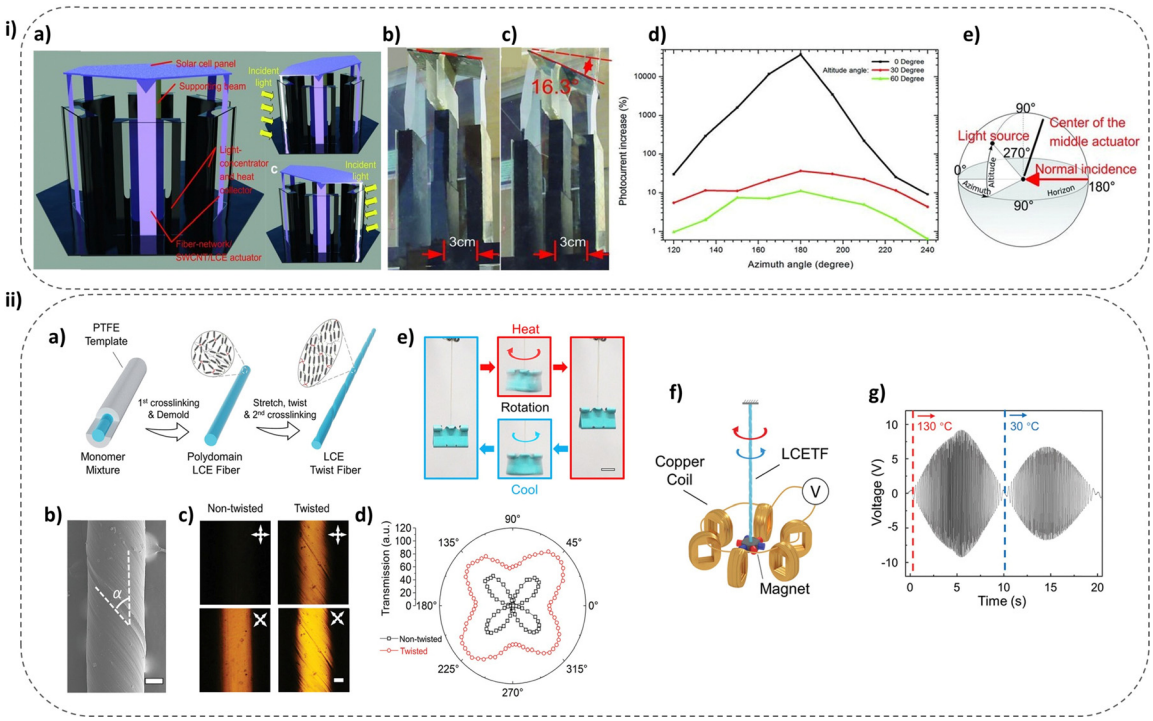

Fig. 12 LCE-based energy harvesters: (i) sun light-responsive artificial heliotropism for enhanced solar energy harvesting: (a) a 3D representation illustrates the heliotropic mechanism, where actuators contract to position the solar cell to face the sun. (b) and (c) An outdoor experiment on August 3, 2011 (43° 4′20″N, 89° 24′44″W) showcased the heliotropic response of a 2-LCHC actuator system. Upon exposure to sunlight, the actuator initiated contraction (b). Within 110 seconds, the actuator achieved full contraction, resulting in a 16.3° tilt of the solar cell (c). (d) Artificial heliotropism using a single LCHC-actuator unit substantially enhanced photocurrent generation. The incident light intensity remained constant at 100 mW cm^{-2}, while its direction was varied. (e) Under the altitude-azimuth coordinate system implemented, the origin was positioned at the actuator's center pointing towards the light, with 0° altitude and 180° azimuth as the normal incidence direction. (ii) LCETF micro-engines: (a) LCETF fabrication using a two-step crosslinking strategy. (b) SEM of LCETF, showcasing the twisted surface structure and twist angle α. The scale bar represents 100 micrometers. (c) POM graphs of LCETF and non-twisted LCE fiber (fiber-axes oriented parallel and at 45°), scale bar: 100 μm. (d) Polarizer angle-dependent light transmission through LCETF and non-twisted LCE fiber. (e) Reversible rotational behavior of LCETF under the influence of a suspended weight during thermal cycling. Scale bar: 1 cm. (f) Schematic of a thermal-driven LCETF electricity generator. (g) The open-circuit voltage generated by the LCETF was measured during thermal cycling (130 °C to 30 °C). (i) Reprinted with permission from ref. 93. Copyright 2012 WILEY-VCH Verlag GmbH & Co. KGaA, Weinheim. (ii) Reprinted with permission from ref. 94. Copyright 2022 Wiley-VCH GmbH.

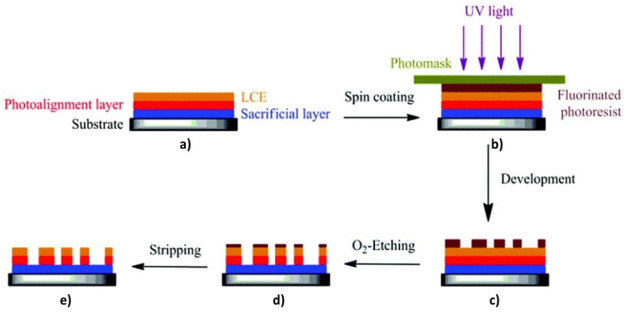

Fig. 13 Patterning using non-mechanical method: (a) on glass or silicon, the sacrificial layer and the photoalignment layer are spin-coated consecutively. (b) The photoresist is patterned using 365-nm UV light and a photomask. (c) The exposed photoresist is then developed using a fluorinated developer, while the unexposed photoresist remains. (d) Next, the LCE film is etched using oxygen plasma treatment, selectively removing the exposed LCE. (e) Finally, the remaining photoresist is removed using a fluorinated stripper. This process produces the desired LCE structures in various shapes, depending on the photomask design. Reprinted (adapted) with permission from ref. 23. Copyright The Royal Society of Chemistry 2017.

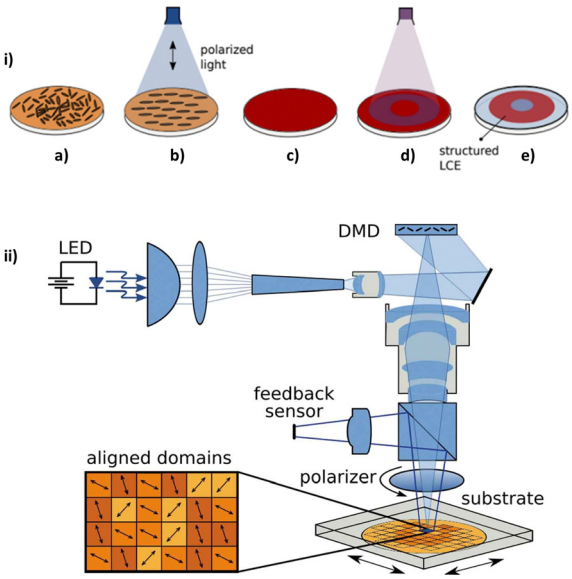

Fig. 14 Selective polymerization using spatially structured light. (i) The sequence of events in this process is as follows: (a) application of BY solution *via* spin-coating onto a glass substrate. (b) Alignment of BY molecules utilizing polarized light. (c) Spin-coating of LC monomer solution. (d) Implementation of selective polymerization to establish the LCE network, accompanied by spatially varied UV light. (e) Development stage, where the unpolymerized network is treated to achieve the desired configuration. (ii) Custom projection setup for reactive mesogen alignment and selective polymerization. (i) Reprinted (adapted) with permission from ref. 98. Copyright 2022, SPIE. (ii) Reprinted (adapted) with permission from ref. 99. Copyright © 2020 The Author(s). Published by Informa UK Limited, trading as Taylor & Francis Group. Distributed under the terms of the Creative Commons Attribution-Non Commercial-No Derivatives License (https://creativecommons.org/licenses/by-nc-nd/4.0/). Minor modification has been made to figure label for improved clarity and consistency.

photoresists compatible with fluorinated LCE solvents.[23] Additionally, a thin photoalignment layer is incorporated, enabling precise *in situ* alignment of mesogens using linearly polarized UV light, eliminating the need for external mechanical techniques. Furthermore, a hard mask of HSQ (hydrogen silsesquioxane) enhances the etch resistance of the LCE film.[23] Fig. 13 illustrates the schematic flow of this process.

5.2 Maskless selective polymerization method

In 2022, Lall and Zappe introduced a novel method for structuring LCE films within glass cells without the need for photomasks.[49,98] This technique, termed maskless photolithography, utilizes light-induced polymerization for the selective patterning of LCE actuators. A commercially available azo-dye, brilliant yellow (BY), serves as the photoalignment layer, directing the alignment of mesogens within the cells.[49] A custom made digital micromirror device (DMD) projects a computer-generated light pattern onto the substrate, inducing the targeted polymerization of the LCE network.[99] Subsequent development removes the non-polymerized regions using a solvent, leaving behind the desired LCE structures within the glass cells.[49] The patterned actuator can be subsequently attached to a 3D-printed substrate *via* a stamp-and-stick bonding process.[49] Fig. 14 depicts the process flow and the specialized DMD-based projection system used in this approach.

5.3 Comparison of methods

The multi-layer spin-coating method offers superior resolution (1.5–2.0 microns[23]) and established compatibility with MEMS technology. However, it necessitates a more complex process flow and relies on specialized materials like fluorinated photoresist and HSQ. Nevertheless, this method empowers the fabrication of micron-sized LCE actuators with precise control over their shape and director orientation. Conversely, the maskless selective polymerization method boasts a simpler and faster process, but with a trade-off in resolution (limited to 1–2 mm[49]) and the requirement for a custom DMD setup. While it leverages a standard glass-cell filling technique, this method does not adequately address scalability concerns for high-volume production. Ultimately, the selection between these techniques hinges on the specific application requirements. If high-resolution, MEMS-compatible actuators are paramount, the multi-layer spin-coating method remains the preferred choice. Conversely, for applications prioritizing simplicity and expeditious fabrication, the maskless approach might be more suitable.

6. Ionic liquid crystal elastomers

iLCEs, recently introduced LCE-based materials,[54] employ electrically induced mass transport of ions or charged species to induce shape changes (or *vice versa*), which exhibits their fundamental operating mechanism.[11] Larger ions moving in one direction stretch the LCE as they require more space. In iLCEs, the direction of deformation is invariant with respect to alignment, whereas the magnitude of deformation is dependent upon alignment.[54] Consequently, by spatially modulating alignment, it is feasible to manipulate and pre-program the

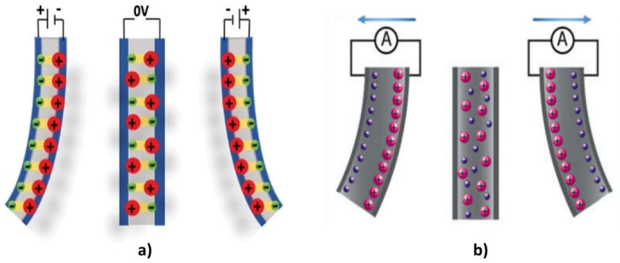

Fig. 15 Schematic illustration of iLCE functionalities. (a) Depicts the actuation mechanism of an iLCE, where an applied electric field induces a shape change. (b) Illustrates the sensor mechanism of an iLCE, where mechanical deformation generates a measurable electrical response (flexo-ionic effect). (a) Reprinted with permission from ref. 54. Copyright 2019 WILEY-VCH Verlag GmbH & Co. KGaA, Weinheim. (b) Reprinted with permission from ref. 100. Copyright 2021 by the authors. Licensee MDPI, Basel, Switzerland. Distributed under the terms and conditions of the Creative Commons Attribution (CC BY) license (https://creativecommons.org/licenses/by/4.0/).

spatial variation of deformation, ranging from zero at defects to maximum at uniform planar alignment.[54]

iLCEs can typically operate at low voltages (less than 1 V for actuation[54]) making them attractive for low-power devices. Within these materials, DC voltages induce ion migration in opposite directions, causing expansion on the side with higher concentrations of larger ions and compression on the opposite side, resulting in substantial bending of thin films.[54] Demonstrating remarkable versatility, iLCEs can function as both actuators and sensors. As actuators, iLCEs can convert electrical stimuli into mechanical deformation, as illustrated schematically in Fig. 15a. Interestingly, iLCEs demonstrate strain sensing behavior in addition to their well-established actuation capabilities. Fig. 15b illustrates the sensing mechanism in iLCE sensors. Feng *et al.* (2019) made a significant contribution by demonstrating the first actuator utilizing the newly developed iLCE (see Fig. 16(i)).[54] The iLCE actuator demonstrated a characteristic oscillation period of 3.5 seconds between its endpoints, primarily governed by the rate of ion migration.[54] The motion exhibited pronounced damping, characterized by a minor overshoot followed by a relaxation time of approximately 20 seconds.[54] This observation underscores the viscoelastic properties of the iLCE actuator.[54] Their innovation opened the door for further exploration of the material's potential, including its sensing capabilities. Sensing functionality arises from the flexo-ionic effect, a phenomenon observed by Rajapaksha *et al.* (2021), where mechanical bending induces a measurable electric current.[100] This effect is essentially the reciprocal of electrically induced bending in iLCE, highlighting the material's unique ability to function as both an actuator and a sensor. In a significant advancement, Rajapaksha *et al.* (2021) revealed that iLCEs exhibit a flexo-ionic effect 157 times larger than flexoelectric effect observed in conventional flexoelectric materials like ceramic lead zirconate titanate (PZTs) at 1 Hz.[100,101] This is because, at low frequencies, the separation of ions within iLCEs due to bending is far more efficient at creating electrical polarization than the movement of bound charges in other materials.[100] This finding

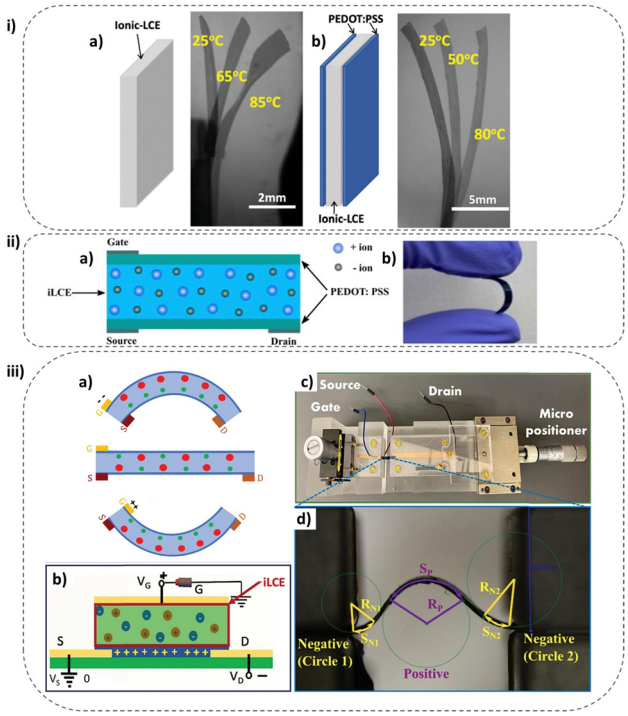

Fig. 16 State-of-the-art iLCE-based devices: (i) iLCE-based actuator: (a) thermal response of a hybrid iLCE sample without electrodes is demonstrated at 25, 65, and 85 °C, highlighting temperature-induced bending. (b) Thermal bending behavior of a hybrid iLCE sample equipped with electrodes is presented at 25, 50, and 80 °C, showcasing the influence of electrodes. (ii) iLCE-based OECT: (a) a schematic diagram of the key components of the iLCE-based OECT (light blue: iLCE-based solid electrolyte. Lower and upper dark green strips: organic semiconductor channel and gate electrode, respectively. Dark gray stripes: copper electrodes). (b) A photograph of the fabricated iLCE-based OECT. The blue appearance originates from the PEDOT:PSS outer layer. (iii) iLCE-based OECT strain sensor: (a) working mechanism of the iLCE-based OECT sensor (G: gate electrode. S: source electrode. D: drain electrode. Larger red dots: positive ions dispersed within the iLCE. Smaller green dots: negative ions dispersed within the iLCE). (b) A schematic representation of the iLCE-OECT device. (c) A top-view image of the sample holder showcases the electrode wires and micro positioners used for alignment and bending actuation. (d) An enlarged view depicting the bent iLCE strip geometry. The local curvatures are denoted as S_{N1}, S_{N2} (negative curvatures at the sides), and S_P (positive curvature in the middle). (i) Reprinted with permission from ref. 54. Copyright 2019 WILEY-VCH Verlag GmbH & Co. KGaA, Weinheim. (ii) Reprinted with permission from ref. 31. Copyright 2022 exclusive license by AIP Publishing. (iii) Reprinted with permission from ref. 103. Copyright © 2023 Informa UK Limited, trading as Taylor & Francis Group.

highlights the exceptional potential of iLCEs for applications requiring high sensitivity transduction mechanisms in low frequencies (less than 1 Hz[102]) like energy harvesters. This finding highlights the exceptional potential of iLCEs for applications requiring high-sensitivity transduction mechanisms in low frequencies (less than 1 Hz[102]) like energy harvesters.

iLCEs, by containing ions within themselves, can significantly enhance their electrical conductivity in addition to their LCE-based characteristics, enabling their actuation through both thermal and electric stimuli. Rajapaksha *et al.* (2022) significantly expanded the functionality of iLCEs by

Table 4 Recent ionic liquids employed in ionic EAP-based devices

Ionic liquid	Abbreviation	Molecular weight (g mol^{-1})	Ref.
1,3-Dimethylimidazolium bis ((trifluoromethyl) sulphonyl) imide	DMIM-TFSI	391.4	107
1-Ethyl-3-methylimidazolium bis(trifluoromethylsulfonyl) imide	EMITFSI	359.24	32, 108
1-Ethyl-3-methylimidazolium trifluoromethanesulfonate	EMI-Tf	260	109
1-Hexyl-3-methylimidazolium hexafluorophosphate	HMIM-PF_6	258.168	54
1-Ethyl-3-methylimidazolium tetrafluoroborate	EMIMBF_4^-	226	110
1-Ethyl-3-methylimidazolium Bromide	EMIMBr	191	106
1-Butyl-3-methylimidazolium hydrogen sulfate	BMIMHS	182.23	111
1-Butyl-3-methylimidazolium tetrafluoroborate	BMIMBF_4^-	171.952	112
1-Butyl 3-methylimidazolium chlorine	BMIMCl	120.60	113

demonstrating their application as OECTs.[31] Exploiting the inherent tunability of the liquid crystal director in iLCEs, they achieved a remarkable g_m/w of 7 S m^{-1}, the highest reported value for any solid-state OECT.[31] Additionally, the switching time of the OECTs with isotropic and planar alignment is observed to be the shortest, approximately 2 seconds.[31] Fig. 16(ii) illustrates both a schematic representation of the OECT components and a photograph of the fabricated device. In a recent development, A. Alyami *et al.* (2023) introduced a highly sensitive directional strain sensor by combining the capabilities of an OECT and an iLCE, which is shown in Fig. 16(iii).[103] This new sensor exhibits remarkable sensitivity, with a potential to increase the drain current by up to four orders of magnitude compared to the flexo-ionic current alone. This enhanced sensitivity is attributed to the amplification of the flexo-ionic current by the OECT, while operating at low voltages ($\sim$1 V). The device demonstrates a sensitivity ranging from 5 to 54 m^{-1} and a response time of 3 s. Further improvements are anticipated by reducing the size of the OECT, potentially achieving a response time of less than 1 s. This ground-breaking work underscores the immense potential of iLCEs for advancements in high-performance organic electronics.

iLCEs hold promise to overcome a major limitation of traditional LCEs, such as slow response[17,19,83,84] and high actuation voltages ($\sim$5 kV[33]), while being able to preserve the advantages, such as tailorable actuation direction and mechanical response. Mirroring LCEs, iLCEs can be preprogrammed to exhibit well-defined actuation patterns by adjusting their mesogen alignment. These exceptional properties position iLCEs as versatile transducers, capable of converting various forms of energy into mechanical motion. Given iLCEs' novelty and limited exploration, their integration into diverse fields like MEMS holds immense potential for driving technological advancements.

6.1 Ionic liquids

The defining characteristic that distinguishes an iLCE from a conventional LCE is the incorporation of ionic liquids. Ionic liquids, a class of salts that exist in liquid form at room temperature, possess remarkable characteristics, including electrochemical stability windows of 4 V or greater, thermal stability up to 400 °C, and very low vapor pressure.[104] Ionic liquids, known for their melting point below room temperature, are composed of a large organic cation and a relatively smaller inorganic or organic anion.[105] Table 4 presents the most recent ionic liquids having seen use in EAP-based devices. To a certain extent, the properties of ionic liquids can be tailored by varying the cation–anion pairings, enabling the creation of customized materials with desired attributes.[105] For instance, Feng *et al.* (2019) investigated how increasing the concentration of an ionic liquid, HMIM-PF6, in an iLCE caused the LC and ionic liquid phases to separate, forming distinct droplet-like structures.[54] As concentration of the ionic liquid in the iLCE is increased, the birefringent areas increased, leading to improved optical properties and electrical conductivity.[54] In addition, the molecular weight of ionic liquids can influence the performance of EAP-based devices. For instance, a study demonstrated that the ion transport properties of polymeric ionic liquids are affected by the polymer molecular weight.[106] As a result, lower-molecular weight can accelerate ion movements, leading to faster device responses.

Biocompatible ionic liquids are being developed for biomedical use by synthesizing them with biocompatible moieties like glucose,[114,115] sweeteners,[116] and amino acids.[117,118] Choline, a biodegradable and water-soluble salt, has been widely used as the cationic component,[119–121] increasing the availability and affordability of these ionic liquids for biomedical applications.[119]

7. Conclusions and perspectives

Amongst soft materials, LCEs have shown the most exciting results for researchers in the field of MEMS, especially in recent years. Their high strain generation (up to 400%[47]), complex deformability,[13,14,28,122] biocompatibility,[123–125] and pre-programmable deformation[126,127] make them particularly attractive for MEMS applications. However, despite these advantages, biocompatible LCEs for biological use remain a relatively limited resource,[123,125,128–131] due to high transition temperatures, complex synthesis, and concerns about biocompatibility.[123] Therefore, careful consideration must be given to the potential challenges associated with using LCEs in biomedical applications.

The integration of LCE as a core MEMS material can be expected to be highly impactful for the development of advanced MEMS devices. Beyond conventional fabrication techniques like molding and capillary filling, two primary methods have been established for integrating LCE into MEMS: multi-layer spin coating and maskless selective polymerization. Multi-layer spin-coating is a MEMS-compatible method using photolithography and etching to create patterned LCE films with precise mesogen alignment.[25] In contrast, maskless selective polymerization avoids photomasks altogether, using light-induced

polymerization with a custom-made DMD projector to directly pattern LCE actuators within glass cells.[49] Either approach is apt to pave the way for widespread LCE adoption as a layer material within complex multi-mask MEMS fabrication technologies.

Furthermore, the emergence of iLCEs has the potential to deeply revolutionize the field of MEMS. Unlike traditional materials like PZT, iLCE offers several advantages that make them highly suitable for MEMS applications. Firstly, they can be actuated electrostatically using low voltages (around 1 V), a more controllable and efficient approach compared to thermal actuation.[45] Secondly, their high flexo-ionic coefficient (at $\sim$1 Hz) translates to superior sensitivity,[100] making them ideal for MEMS sensors. Thirdly, iLCE actuators offer a significant advantage over conventional LCE actuators in terms of response time. While traditional LCEs typically exhibit response times in the tens of seconds,[47,83,88,89,132] iLCE actuators have demonstrated a swing time of only 3.5 seconds[54] (swing time refers to the time it takes for the iLCE to travel from one end to the other). This rapid response is attributed to accelerated ion migration within ionic liquids.[54] Beyond the manipulation of different ionic liquids, other strategies can enhance the response time of iLCE actuators. For instance, Liu *et al.* (2010) demonstrated the significant role of porous electrode structures in improving actuation speed in ionic EAPs.[133] By reducing the thickness of these electrodes, such as layer-by-layer (LbL) self-assembled gold nanoparticle composites, ion transport time can be minimized, leading to faster actuation and improved energy efficiency. Their ionic EAP actuator, featuring a LbL porous composite electrode layer thickness of 0.4 μm, achieved a remarkable actuation response time of approximately 0.18 seconds. This suggests that iLCE actuators with optimized porous electrode structures have the potential for even faster response times and higher electromechanical strain, making them well-suited for applications requiring rapid and efficient actuation.

These combined factors position iLCEs as ideal candidates for actuation, sensing, and energy harvesting applications within MEMS technology. The low-voltage electrostatic actuation mechanism inherent to iLCEs presents a significant advantage for MEMS applications. Unlike traditional LCEs that require high voltages (typically several kV) for actuation, iLCEs can be actuated using low voltages while still generating sufficient strain. This translates to lower power consumption for the MEMS device and a simpler design for the driving circuitry, making iLCEs particularly well-suited for integration into MEMS devices.

By integrating iLCE into MEMS, researchers can develop diverse soft sensors for continuous measurements, as well as actuators for precise control and manipulation tasks. These sensors offer the potential for continuous measurement of a wide range of parameters, including pressure, strain, shear, and temperature. iLCE actuators, on the other hand, with their capacity for precise control and high generated strain, are ideally suited for applications requiring delicate manipulation, including micromirrors, optical switches, micro positioners, microvalves, and micropumps. The integration of such sensors and actuators with microcircuits lays the foundation for soft bioelectronics, paving the way for innovative medical devices, robots, and wearable electronics. However, challenges remain. Developing precise and compatible fabrication processes that seamlessly integrate iLCEs with MEMS devices without compromising their properties is crucial. Also, the successful deployment of iLCEs in biomedical contexts hinges upon the thorough evaluation and mitigation of biocompatibility challenges related to LCE precursors, ionic liquids, and actuation/sensing mechanisms. Additionally, future efforts should focus on designing iLCE-based MEMS devices with minimal energy consumption and the ability to operate through *in situ* actuation, further expanding their potential.

Data availability

No primary research results, software or codes have been included and no new data were generated or analysed as part of this review.

Conflicts of interest

There are no conflicts to declare.

Acknowledgements

The authors are grateful for the invaluable support and guidance provided by Professor Antal Jakli of the Advanced Materials and Liquid Crystal Institute, Kent State University, USA. The authors acknowledge the financial support provided by the Natural Sciences and Engineering Research Council of Canada (NSERC) and the Regroupement Stratégique en Microsystèmes du Québec (ReSMiQ), as well as the infrastructure access and support provided by the Laboratoire de communications et d'intégration de la microélectronique (LACIME).

References

1 D.-H. Kim, N. Lu, Y. Huang and J. A. Rogers, *MRS Bull.*, 2012, **37**, 226–235.
2 T. Mirfakhrai, J. D. Madden and R. H. Baughman, *Mater. Today*, 2007, **10**, 30–38.
3 C. Parameswaran and D. Gupta, *Nano Convergence*, 2019, **6**, 1–23.
4 A. R. Aiyar, C. Song, S.-H. Kim and M. G. Allen, *Smart Mater. Struct.*, 2009, **18**, 115002.
5 X. Yang and M. Zhang, *Nanotechnol. Precis. Eng.*, 2021, **4**, 025001.
6 D. Thuau, C. Ayela, E. Lemaire, S. Heinrich, P. Poulin and I. Dufour, *Mater. Horiz.*, 2015, **2**, 106–112.
7 C. Liu, *Adv. Mater.*, 2007, **19**, 3783–3790.
8 W. Zhang, K. Jin, Z. Ren, L. Li, L. Chang, C. Zhang, R. Wang, B. Li, G. Wu and Y. Hu, *Adv. Funct. Mater.*, 2024, 2408496.

9 S. Chen, S. F. Tan, H. Singh, L. Liu, M. Etienne and P. S. Lee, *Adv. Mater.*, 2024, **36**, 2307045.
10 Y. Bar-Cohen, *Electroactive Polymer (EAP) Actuators as Artificial Muscles: Reality, Potential, and Challenges*, SPIE Press, Bellingham, Washington USA, 2004.
11 R. D. Kornbluh, R. Pelrine, H. Prahlad and R. Heydt, Electroactive polymers: an emerging technology for MEMS, Proc. SPIE 5344, MEMS/MOEMS Components and Their Applications, 2004, DOI: 10.1117/12.538382.
12 V. Guarino, S. Zuppolini, A. Borriello and L. Ambrosio, *Polymers*, 2016, **8**, 185.
13 H. Zeng, O. M. Wani, P. Wasylczyk, R. Kaczmarek and A. Priimagi, *Adv. Mater.*, 2017, **29**, 1701814.
14 S. Schuhladen, F. Preller, R. Rix, S. Petsch, R. Zentel and H. Zappe, *Adv. Mater.*, 2014, **26**, 7247–7251.
15 A. Sánchez-Ferrer, T. Fischl, M. Stubenrauch, H. Wurmus, M. Hoffmann and H. Finkelmann, *Macromol. Chem. Phys.*, 2009, **210**, 1671–1677.
16 S. Eom, K. Miyata, K. Asai, J.-W. Kim and K. Yoshida, *presented in part at Electroactive Polymer Actuators and Devices (EAPAD) 2017*, Portland, Oregon, United States, Apr 17, 2017.
17 S. Haefner, R. Koerbitz, P. Frank, M. Elstner and A. Richter, *Adv. Mater. Technol.*, 2018, **3**, 1700108.
18 Y. Yu and T. Ikeda, *Angew. Chem., Int. Ed.*, 2006, **45**, 5416–5419.
19 L. Dong, A. K. Agarwal, D. J. Beebe and H. Jiang, *Nature*, 2006, **442**, 551–554.
20 J. D. Carrico, K. J. Kim and K. K. Leang, *presented in part at 2017 IEEE International Conference on Robotics and Automation (ICRA)*, Singapore, May 29–June 3, 2017.
21 N. Terasawa, *Langmuir*, 2020, **36**, 6154–6159.
22 H. Phung, C. T. Nguyen, H. Jung, T. D. Nguyen and H. R. Choi, *Smart Mater. Struct.*, 2020, **29**, 035007.
23 D. Ditter, W.-L. Chen, A. Best, H. Zappe, K. Koynov, C. K. Ober and R. Zentel, *J. Mater. Chem. C*, 2017, **5**, 12635–12644.
24 A. Sánchez-Ferrer, N. Torras and J. Esteve, *Liq. Cryst. Polym.*, 2016, 553–582.
25 D. Ditter, W. L. Chen, A. Best, H. Zappe, K. Koynov, C. K. Ober and R. Zentel, *J. Mater. Chem. C*, 2017, **5**(47), 12635–12644.
26 C. P. Ambulo, J. J. Burroughs, J. M. Boothby, H. Kim, M. R. Shankar and T. H. Ware, *ACS Appl. Mater. Interfaces*, 2017, **9**, 37332–37339.
27 T. H. Ware, J. S. Biggins, A. F. Shick, M. Warner and T. J. White, *Nat. Commun.*, 2016, **7**, 10781.
28 S. Iamsaard, S. J. Aßhoff, B. Matt, T. Kudernac, J. J. Cornelissen, S. P. Fletcher and N. Katsonis, *Nat. Chem.*, 2014, **6**, 229–235.
29 T. J. White and D. J. Broer, *Nat. Mater.*, 2015, **14**, 1087–1098.
30 T. Ware and T. White, *Polym. Chem.*, 2015, **6**, 4835–4844.
31 C. Hemantha Rajapaksha, P. R. Paudel, P. Kodikara, D. Dahal, T. M. Dassanayake, V. Kaphle, B. Lüssem and A. Jákli, *Appl. Phys. Rev.*, 2022, **9**, 011415.
32 Y. Deng, G. Liu, A. Brulet, G. T. Nguyen, D. Dudzinski, F. Vidal, C. Plesse, C. Vancaeyzeele and M. H. Li, *Adv. Funct. Mater.*, 2024, 2403892.
33 M.-Y. Choi, K. Kim, K. Kim, S.-K. Ahn and J.-H. Na, *Chem. Eng. J.*, 2023, **475**, 146237.
34 F. Ge and Y. Zhao, *Adv. Funct. Mater.*, 2020, **30**, 1901890.
35 P. de Gennes, *Oxford Clarendon Press google schola*, 1993, vol. 2, pp. 1625–1627.
36 K. M. Herbert, H. E. Fowler, J. M. McCracken, K. R. Schlafmann, J. A. Koch and T. J. White, *Nat. Rev. Mater.*, 2022, **7**, 23–38.
37 S. W. Ula, N. A. Traugutt, R. H. Volpe, R. R. Patel, K. Yu and C. M. Yakacki, *Liq. Cryst. Rev.*, 2018, **6**, 78–107.
38 P.-G. De Gennes and J. Prost, *The physics of liquid crystals*, Oxford University Press, 1993.
39 A. M. Menzel, *Phys. Rep.*, 2015, **554**, 1–45.
40 M. Simoes and D. Simeao, *Phys. Rev. E: Stat., Nonlinear, Soft Matter Phys.*, 2006, **74**, 051701.
41 F. Brömmel, D. Kramer and H. Finkelmann, *Liquid crystal elastomers: materials and applications*, 2012, pp. 1–48.
42 C. Ohm, M. Brehmer and R. Zentel, *Adv. Mater.*, 2010, **22**, 3366–3387.
43 M. Warner and E. M. Terentjev, *Liquid Crystal Elastomers*, Oxford University Press, 2003.
44 M. Warner and E. Terentjev, *Prog. Polym. Sci.*, 1996, **21**, 853–891.
45 Y.-Y. Xiao, Z.-C. Jiang, J.-B. Hou, X.-S. Chen and Y. Zhao, *Soft Matter*, 2022, **18**, 4850–4867.
46 D. Rogez, S. Krause and P. Martinoty, *Soft Matter*, 2018, **14**, 6449–6462.
47 A. Sánchez-Ferrer and H. Finkelmann, *Mol. Cryst. Liq. Cryst.*, 2009, **508**, 348–356.
48 F. Zander and H. Finkelmann, *Macromol. Chem. Phys.*, 2010, **211**, 1167–1176.
49 J. Lall and H. Zappe, *Smart Mater. Struct.*, 2022, **31**, 115014.
50 Y. J. Lee, M. K. Abdelrahman, M. S. Kalairaj and T. H. Ware, *Small*, 2023, 2302774.
51 X. Wang, H. Shao, J. Tang, J. Chen, Y. Huang, J. Pan, Y. Zhang, W. Wang, J. Jiang and N. Chen, *Adv. Mater. Technol.*, 2023, 2300814.
52 J. Shin, M. Kang, T. Tsai, C. Leal, P. V. Braun and D. G. Cahill, *ACS Macro Lett.*, 2016, **5**, 955–960.
53 H. Liang, Y.-W. Liu, H.-T. Xu, Y. Yang, E.-J. He, Z. Yang, Y. Wei and Y. Ji, *Chin. J. Polym. Sci.*, 2023, **41**, 1656–1662.
54 C. Feng, C. P. H. Rajapaksha, J. M. Cedillo, C. Piedrahita, J. Cao, V. Kaphle, B. Lüssem, T. Kyu and A. Jákli, *Macromol. Rapid Commun.*, 2019, **40**, 1900299.
55 K. D. Harris, R. Cuypers, P. Scheibe, C. L. van Oosten, C. W. Bastiaansen, J. Lub and D. J. Broer, *J. Mater. Chem.*, 2005, **15**, 5043–5048.
56 G. N. Mol, K. D. Harris, C. W. Bastiaansen and D. J. Broer, *Adv. Funct. Mater.*, 2005, **15**, 1155–1159.
57 H. Jiang, C. Li and X. Huang, *Nanoscale*, 2013, **5**, 5225–5240.
58 M. Hussain, E. I. Jull, R. J. Mandle, T. Raistrick, P. J. Hine and H. F. Gleeson, *Nanomaterials*, 2021, **11**, 813.

59 B. Donnio, H. Wermter and H. Finkelmann, *Macromolecules*, 2000, **33**, 7724–7729.
60 J. Zhao, L. Zhang and J. Hu, *Adv. Intell. Syst.*, 2022, **4**, 2100065.
61 L. Pohl, R. Eidenschink, J. Krause and G. Weber, *Phys. Lett. A*, 1978, **65**, 169–172.
62 O. Yaroshchuk and Y. Reznikov, *J. Mater. Chem.*, 2012, **22**, 286–300.
63 M. Obi, S. Y. Morino and K. Ichimura, *Jpn. J. Appl. Phys.*, 1999, **38**, L145.
64 M. Obi, S. Y. Morino and K. Ichimura, *Macromol. Rapid Commun.*, 1998, **19**, 643–646.
65 P. O. Jackson, M. O'Neill, W. L. Duffy, P. Hindmarsh, S. M. Kelly and G. J. Owen, *Chem. Mater.*, 2001, **13**, 694–703.
66 S. Kumar, J.-H. Kim and Y. Shi, *Phys. Rev. Lett.*, 2005, **94**, 077803.
67 T. Seki, M. Sakuragi, Y. Kawanishi, T. Tamaki, R. Fukuda, K. Ichimura and Y. Suzuki, *Langmuir*, 1993, **9**, 211–218.
68 Y. Xia, G. Cedillo-Servin, R. D. Kamien and S. Yang, *Adv. Mater.*, 2016, **28**, 9637–9643.
69 T. Ikeda, J. i Mamiya and Y. Yu, *Angew. Chem., Int. Ed.*, 2007, **46**, 506–528.
70 M.-H. Li and P. Keller, *Philos. Trans. R. Soc., A*, 2006, **364**, 2763–2777.
71 A. Jakli, *Liq. Cryst.*, 2010, **37**, 825–837.
72 D. L. Thomsen, P. Keller, J. Naciri, R. Pink, H. Jeon, D. Shenoy and B. R. Ratna, *Macromolecules*, 2001, **34**, 5868–5875.
73 Y. Yusuf, P. Cladis, H. R. Brand, H. Finkelmann and S. Kai, *Chem. Phys. Lett.*, 2004, **389**, 443–448.
74 S. Petsch, B. Khatri, S. Schuhladen, L. Köbele, R. Rix, R. Zentel and H. Zappe, *Smart Mater. Struct.*, 2016, **25**, 085010.
75 A. Komp, J. Rühe and H. Finkelmann, *Macromol. Rapid Commun.*, 2005, **26**, 813–818.
76 A. Hotta and E. Terentjev, *Eur. Phys. J. E*, 2003, **10**, 291–301.
77 A. Komp and H. Finkelmann, *Macromol. Rapid Commun.*, 2007, **28**, 55–62.
78 C. Yakacki, M. Saed, D. Nair, T. Gong, S. Reed and C. Bowman, *RSC Adv.*, 2015, **5**, 18997–19001.
79 F.-H. Lin, C.-Y. Ho and J.-Y. Lee, *Opt. Mater.*, 2012, **34**, 1181–1194.
80 Y. Yu, M. Nakano and T. Ikeda, *Nature*, 2003, **425**, 145.
81 J. Chen, D. Johnson, P. J. Bos, S. Sprunt, J. Lando and J. MannJr, *Appl. Phys. Lett.*, 1996, **68**, 885–887.
82 A. Buguin, M.-H. Li, P. Silberzan, B. Ladoux and P. Keller, *J. Am. Chem. Soc.*, 2006, **128**, 1088–1089.
83 A. Sánchez-Ferrer, T. Fischl, M. Stubenrauch, A. Albrecht, H. Wurmus, M. Hoffmann and H. Finkelmann, *Adv. Mater.*, 2011, **23**, 4526–4530.
84 Q. He, Z. Wang, Y. Wang, A. Minori, M. T. Tolley and S. Cai, *Sci. Adv.*, 2019, **5**, eaax5746.
85 Q. He, Z. Wang, Y. Wang, Z. Song and S. Cai, *ACS Appl. Mater. Interfaces*, 2020, **12**, 35464–35474.
86 J. Min, Z. Wu, W. Zhang, Y. Liu and D. Luo, *Adv. Sens. Res.*, 2024, **3**, 2300117.
87 Z. Liang, B. Jin, H. Zhao, Z. He, Z. Jiang and S. Jiang, *Small*, 2024, **20**, 2305371.
88 L.-Y. Lo, P.-T. Lin, C.-Y. Cho, H.-Y. Wang and Y.-J. Yang, *presented in part at 2024 IEEE 37th International Conference on Micro Electro Mechanical Systems (MEMS)*, Austin, TX, USA, 21–25 January, 2024.
89 K. Zheng, B. Tian, P. Guo, H. Zhan, J. Liang, Y. Wu and W. Wu, *Chem. Eng. J.*, 2024, **492**, 152172.
90 Y.-L. Chi, W.-Y. Wang and Y.-J. Yang, *Sens. Actuators, A*, 2024, **370**, 115257.
91 M. Brundel, *MST News*, 2004, **4**, 38.
92 L. Li, W. Zhang, Z. Ren, L. Chang, X. Xu and Y. Hu, *Chem. Eng. J.*, 2023, 147550.
93 C. Li, Y. Liu, X. Huang and H. Jiang, *Adv. Funct. Mater.*, 2012, **22**, 5166–5174.
94 Y. Wang, J. Sun, W. Liao and Z. Yang, *Adv. Mater.*, 2022, **34**, 2107840.
95 A. Kotikian, R. L. Truby, J. W. Boley, T. J. White and J. A. Lewis, *Adv. Mater.*, 2018, **30**, 1706164.
96 X. Liu, S.-K. Kim and X. Wang, *J. Mater. Chem. B*, 2016, **4**, 7293–7302.
97 Z. L. Wu, A. Buguin, H. Yang, J. M. Taulemesse, N. Le Moigne, A. Bergeret, X. Wang and P. Keller, *Adv. Funct. Mater.*, 2013, **23**, 3070–3076.
98 J. Lall and H. Zappe, Structuring of liquid crystal elastomer actuators with selective polymerization for MEMS devices, presented in part at Advanced Fabrication Technologies for Micro/Nano Optics and Photonics XV, San Francisco, California, United States, 5 March, 2022.
99 Y. Folwill, Z. Zeitouny, J. Lall and H. Zappe, *Liq. Cryst.*, 2021, **48**, 862–872.
100 C. H. Rajapaksha, M. T. Gunathilaka, S. Narute, H. Albehaijan, C. Piedrahita, P. Paudel, C. Feng, B. Lüssem, T. Kyu and A. Jákli, *Molecules*, 2021, **26**, 4234.
101 W. Ma and L. E. Cross, *Appl. Phys. Lett.*, 2005, **86**(7), 072905.
102 A. Alyami, C. H. Rajapaksha, C. Feng, P. R. Paudel, A. Paul, A. Adaka, R. Dharmarathna, B. Lüssem and A. Jákli, *Liq. Cryst.*, 2023, **50**, 1151–1161.
103 A. Alyami, C. H. Rajapaksha, P. R. Paudel, V. Kaphle, S. G. Kodikara, B. Lüssem and A. Jákli, *Liq. Cryst.*, 2024, **51**, 297–304.
104 B. J. Akle, M. D. Bennett and D. J. Leo, *Sens. Actuators, A*, 2006, **126**, 173–181.
105 C. P. H. Rajapaksha, *Ionic Electroactive Polymers and Liquid Crystal Elastomers for Applications in Soft Robotics, Energy Harvesting, Sensing and Organic Electrochemical Transistors*, Kent State University, 2022.
106 M. J. Kim, S. W. Park, J. Won and C. Nah, *presented in part at Electroactive Polymer Actuators and Devices (EAPAD) 2017*, Portland, Oregon, United States, Apr 17, 2017.
107 A. Alyami, C. H. Rajapaksha, C. Feng, P. R. Paudel, A. Paul, A. Adaka, R. Dharmarathna, B. Lüssem and A. Jákli, *Liq. Cryst.*, 2023, 1–11.
108 V. Woehling, G. T. Nguyen, C. Plesse, Y. Petel, Y. Dobashi, J. D. Madden, C. A. Michal and F. Vidal, *Multifunct. Mater.*, 2019, **2**, 045002.

109 A. Almomani, W. Hong, W. Hong and R. Montazami, *Polymers*, 2017, **9**, 358.
110 D. Guo, Y. Han, J. Huang, E. Meng, L. Ma, H. Zhang and Y. Ding, *ACS Appl. Mater. Interfaces*, 2019, **11**, 2386–2397.
111 V. Panwar, S. Mohanty, G. Anoop and S. Kumar, *Sens. Actuators, A*, 2020, **315**, 112277.
112 M. A. Montiel, J. Solla-Gullón and C. M. Sánchez-Sánchez, *J. Solid State Electrochem.*, 2016, **20**, 1043–1052.
113 Y. Liu, C. Lu, S. Twigg, M. Ghaffari, J. Lin, N. Winograd and Q. Zhang, *Sci. Rep.*, 2013, **3**, 973.
114 L. Poletti, C. Chiappe, L. Lay, D. Pieraccini, L. Polito and G. Russo, *Green Chem.*, 2007, **9**, 337–341.
115 S. Jopp, T. Fleischhammer, A. Lavrentieva, S. Kara and J. Meyer, *RSC Sustainability*, 2023, **1**, 1751–1764.
116 P. Nockemann, B. Thijs, K. Driesen, C. R. Janssen, K. Van Hecke, L. Van Meervelt, S. Kossmann, B. Kirchner and K. Binnemans, *J. Phys. Chem. B*, 2007, **111**, 5254–5263.
117 G.-h Tao, L. He, N. Sun and Y. Kou, *Chem. Commun.*, 2005, 3562–3564.
118 S. Kirchhecker and D. Esposito, *Curr. Opin. Green Sustainable Chem.*, 2016, **2**, 28–33.
119 B. L. Gadilohar and G. S. Shankarling, *J. Mol. Liq.*, 2017, **227**, 234–261.
120 D.-J. Tao, Z. Cheng, F.-F. Chen, Z.-M. Li, N. Hu and X.-S. Chen, *J. Chem. Eng. Data*, 2013, **58**, 1542–1548.
121 F. Pena-Pereira, A. Kloskowski and J. Namieśnik, *Green Chem.*, 2015, **17**, 3687–3705.
122 J. Zhang, Y. Wang, Y. Sun, S. Sun, Z. Xu, J. Li, J. Li and X. Gong, *ACS Appl. Poly. Mater.*, 2023, **5**, 6199–6211.
123 C. Ferrantini, J. M. Pioner, D. Martella, R. Coppini, N. Piroddi, P. Paoli, M. Calamai, F. S. Pavone, D. S. Wiersma and C. Tesi, *Circ. Res.*, 2019, **124**, e44–e54.
124 M. E. Prévôt, S. Ustunel and E. Hegmann, *Materials*, 2018, **11**, 377.
125 A. Agrawal, H. Chen, H. Kim, B. Zhu, O. Adetiba, A. Miranda, A. Cristian Chipara, P. M. Ajayan, J. G. Jacot and R. Verduzco, *ACS Macro Lett.*, 2016, **5**, 1386–1390.
126 S. Li, M. Aizenberg, M. M. Lerch and J. Aizenberg, *Acc. Mater. Res.*, 2023, **4**, 1008–1019.
127 G. Chen, B. Jin, Y. Shi, Q. Zhao, Y. Shen and T. Xie, *Adv. Mater.*, 2022, **34**, 2201679.
128 A. Agrawal, O. Adetiba, H. Kim, H. Chen, J. G. Jacot and R. Verduzco, *J. Mater. Res.*, 2015, **30**, 453–462.
129 T. Bera, E. J. Freeman, J. A. McDonough, R. J. Clements, A. Aladlaan, D. W. Miller, C. Malcuit, T. Hegmann and E. Hegmann, *ACS Appl. Mater. Interfaces*, 2015, **7**, 14528–14535.
130 Y. Gao, T. Mori, S. Manning, Y. Zhao, A. D. Nielsen, A. Neshat, A. Sharma, C. J. Mahnen, H. R. Everson and S. Crotty, *ACS Macro Lett.*, 2016, **5**, 4–9.
131 D. Martella and C. Parmeggiani, *Chem. – Eur. J.*, 2018, **24**, 12206–12220.
132 Q. He, Z. Wang, Y. Wang, A. Minori, M. Tolley and S. Cai, *Sci. Adv.*, 2019, **5**, eaax5746.
133 S. Liu, R. Montazami, Y. Liu, V. Jain, M. Lin, X. Zhou, J. R. Heflin and Q. Zhang, *Sens. Actuators, A*, 2010, **157**, 267–275.